Leading in Education, Research and Decision Support
Competence Center Environment and Sustainability
COGEAR: COupled seismogenic GEohazards in Alpine Regions

COGEAR

MODULE 2:

Earthquake Ground Motion Simulation (Kinematic and dynamic rupture models)

Del. No.: 2a.3

Authors: Dalguer L.A., Song S.G., and Baumann C.

Swiss Seismological Service

SED/COGEAR/R/009/20120712
July 12, 2012

Project Report: COGEAR, Module 2

Task 2a.3 Earthquake Ground Motion Simulation (Kinematic and dynamic rupture models)

Content:

-Source Characterization – Kinematic modeling (by Seok Goo Song and Luis A. Dalguer)

-Dynamic rupture models and ground motion simulations (By Cyrill Baumann)

-Synthetic broadband ground motion database of two normal faulting models for Visp Area (By Luis A. Dalguer)

Project Report: COGEAR, Module 2

Seok Goo Song and Luis Angel Dalguer

Source Characterization – Kinematic modeling

Complex finite faulting source processes can affect near-source ground motions significantly. In general empirical ground motion prediction approaches suffer from the lack of data in near-source regions. Simulation-based approaches can provide us with some insights into near-source ground motion characteristics, but it is still a difficult task to generate physics-based rupture scenarios, compatible with potential future events in a certain region. Spontaneous dynamic rupture modeling has been considered a promising tool to provide physical constraints in earthquake source modeling for simulating ground motions. However we are still limited to constraining dynamic input parameters such as stress drop and fracture energy and also to understanding frictional behaviors during earthquake rupture. In addition the dynamic modeling is computationally very expensive. On the other hand, pseudo-dynamic modeling keeps the computational efficiency of kinematic modeling, and tries to emulate the essential physics of source process inferred from rupture dynamics (Guatteri et al., 2004; Schmedes et al., 2010; Song and Somerville, 2010; Mena et al., 2012). The source modeling scheme adopted in this study shares the same philosophy with the pseudo-dynamic modeling approaches, but finite source processes are formulated with a spatial random field model which is defined with 1-point and 2-point statistics of kinematic source parameters as illustrated in Figure 1. 1-point statistics represents a marginal probability density function (mPDF) for a certain source parameter at a given point while 2-point statistics contains both auto- and cross-correlation structures for source parameters as a function of separation vector, **h**. Both 1-point and 2-point statistics in the spatial random field model can be constrained by dynamic rupture modeling and finite source inversion, which implies that the random field model has both physical and data constraints.

Dalguer (2011) constructs a set of dynamic rupture models for physics-based source and ground motion modeling in the Visp area. The database contains 360 events with a magnitude range of M_w 5.5 – 7.0. The events are composed of three types of faulting (strike-slip, normal, and thrust faulting) for both buried and surface rupturing events. Both depth-dependent and independent normal stresses are implemented, which controls the depth-dependency of initial stress and frictional strength in the modeling. The objective of this study is to extract main statistical features, i.e., 1-point and 2-point statistics of source parameters, from the dynamic rupture models for the Visp area and to perform pseudo-dynamic modeling and test whether the pseudo-dynamic source modeling with the spatial random field model inferred from dynamic rupture models can produce near-source ground motions, consistent with ground motions generated from the full dynamic modeling.

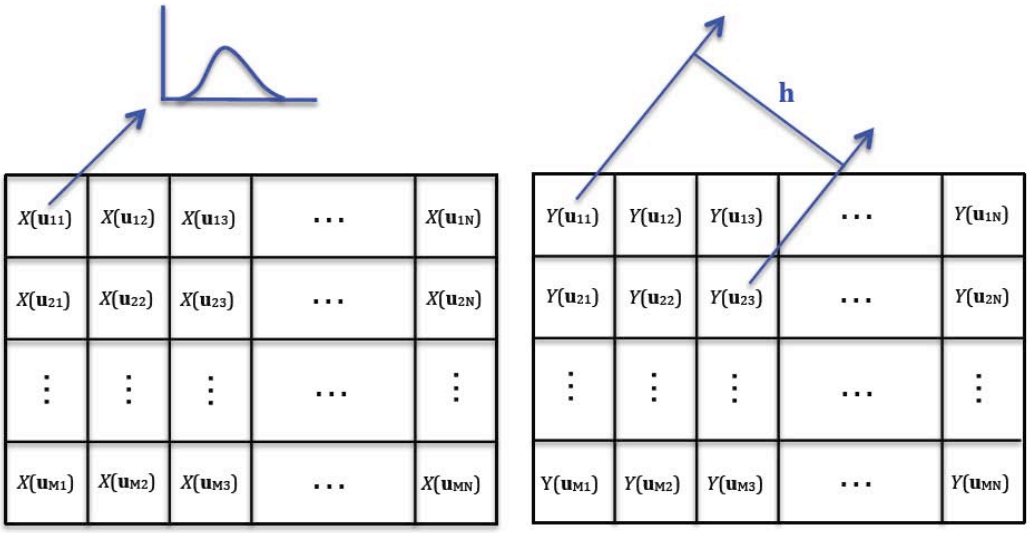

Figure 1. Spatial random field model that characterizes finite faulting source processes by assigning a set of random variables (or random field) to each kinematic source parameter such as slip, rupture velocity, etc. The random field, $X(\mathbf{u})$, is assigned to earthquake slip and, the random field, $Y(\mathbf{u})$, is assigned to rupture velocity, and so on. $\mathbf{u}$ is a location vector, and $\mathbf{h}$ is a separation vector between two random variables, for instance, between $Y(\mathbf{u}_{11})$ and $Y(\mathbf{u}_{23})$. In principle, the random field model should be defined with a complete description of multi-variate probability density function, but in most practical applications, we are limited to constraining its 1-point and 2-point statistics, i.e., a marginal probability density function (mPDF) at a given point (see an example for $X(\mathbf{u}_{11})$) and both auto- and cross-correlation structures as a function of the separation vector, $\mathbf{h}$.

Figure 2 shows an example of dynamic rupture model extracted from the rupture model database (Dalguer, 2011). It is a normal faulting event with M_w 6.5 and it has no surface rupture. Depth-dependent normal stress is implemented in the model. Because of the depth-dependent input parameters in the rupture modeling, we can observe that kinematic parameters (slip, rupture velocity, and peak slip velocity) also vary with depth and show peaks around 13 km in the along-dip direction. As summarized in Figure 3, both 1-point variability and 2-point auto- and cross-correlation structures are extracted from the model, based on the method introduced in Song et al. (2009) and Song and Somerville (2010). From the bottom panel of Figure 3a, we can clearly confirm that the 1-point variability of kinematic source parameters, i.e., mean and variance, significantly changes as a function of depth. We decide to implement the depth-dependency (or non-stationarity of 1-point variability) in the pseudo-dynamic modeling.

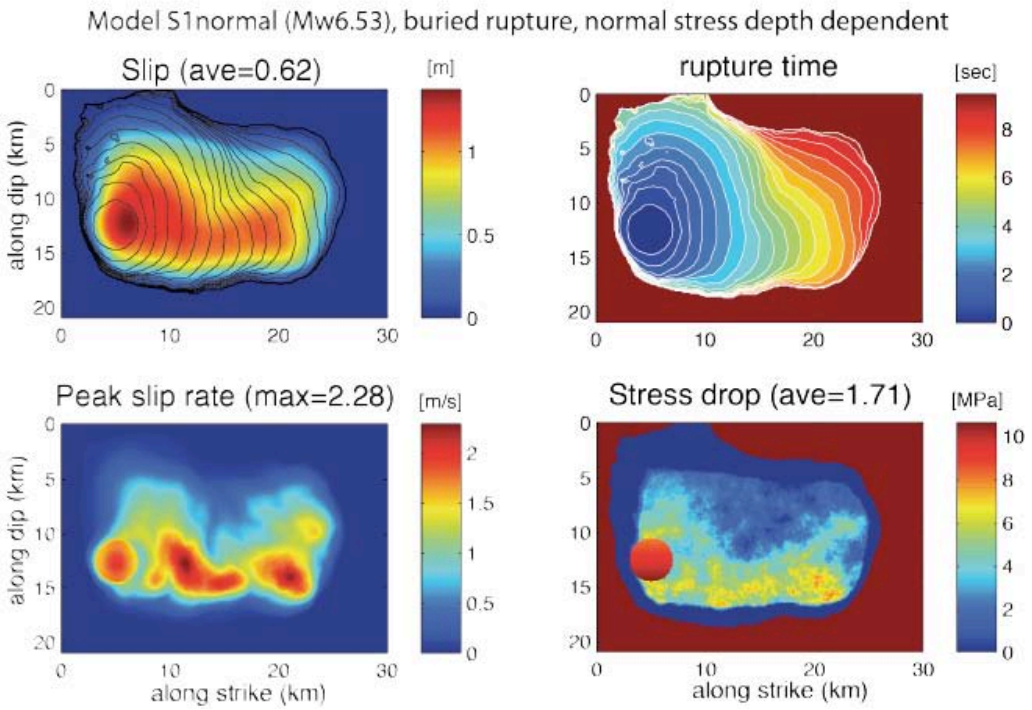

Figure 2. An example of dynamic rupture model for the Visp area (Dalguer, 2011).

Figure 3b shows both 2-point auto- and cross-correlation structures extracted from the dynamic model in Figure 2. 2-point autocorrelation for both slip and peak slip velocity shows correlation patterns significantly elongated in the along-strike direction while autocorrelation for rupture velocity shows an isotropic decay pattern. Regarding cross-correlations between source parameters (off-diagonal panels in Figure 3b), strong correlations (0.5 ~ 0.8) are observed between all parameters at zero-offset distance (**h** = 0). The decay patterns as the separation vector, **h**, perturbs, are slightly different. For example, the decay rate is slower in the forward rupture direction than in the backward rupture direction for the cross-correlation between slip and rupture velocity while they are roughly symmetric between slip and peak slip velocity and between rupture velocity and peak slip velocity.

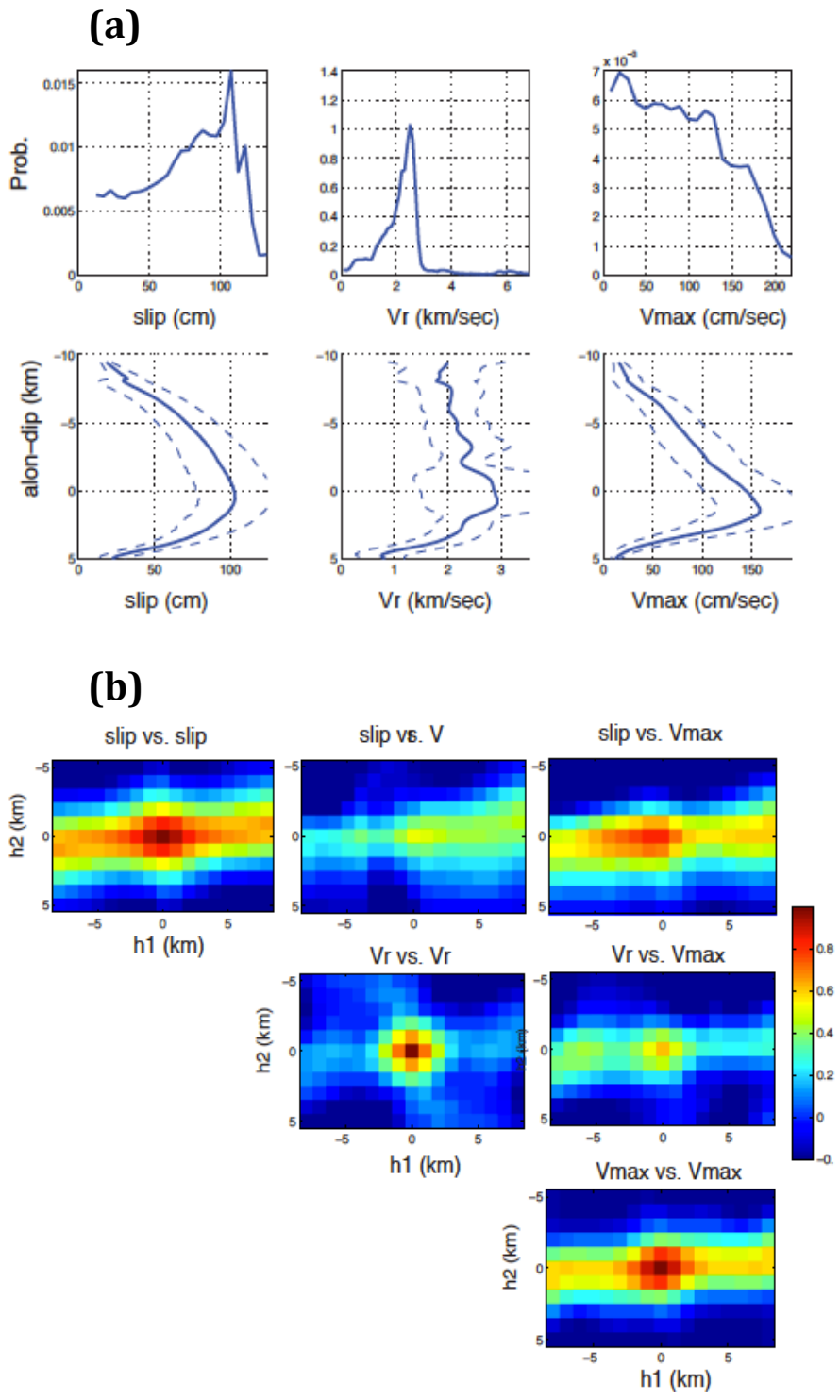

Figure 3. (a) 1-point and (b) 2-point statistics extracted from the dynamic model in Figure 2. The 1-point variability for kinematic source parameters has strong depth-dependency as shown in the bottom panel of (a). The kinematic source parameters are also strongly correlated with one another as observed in the cross-correlograms in (b).

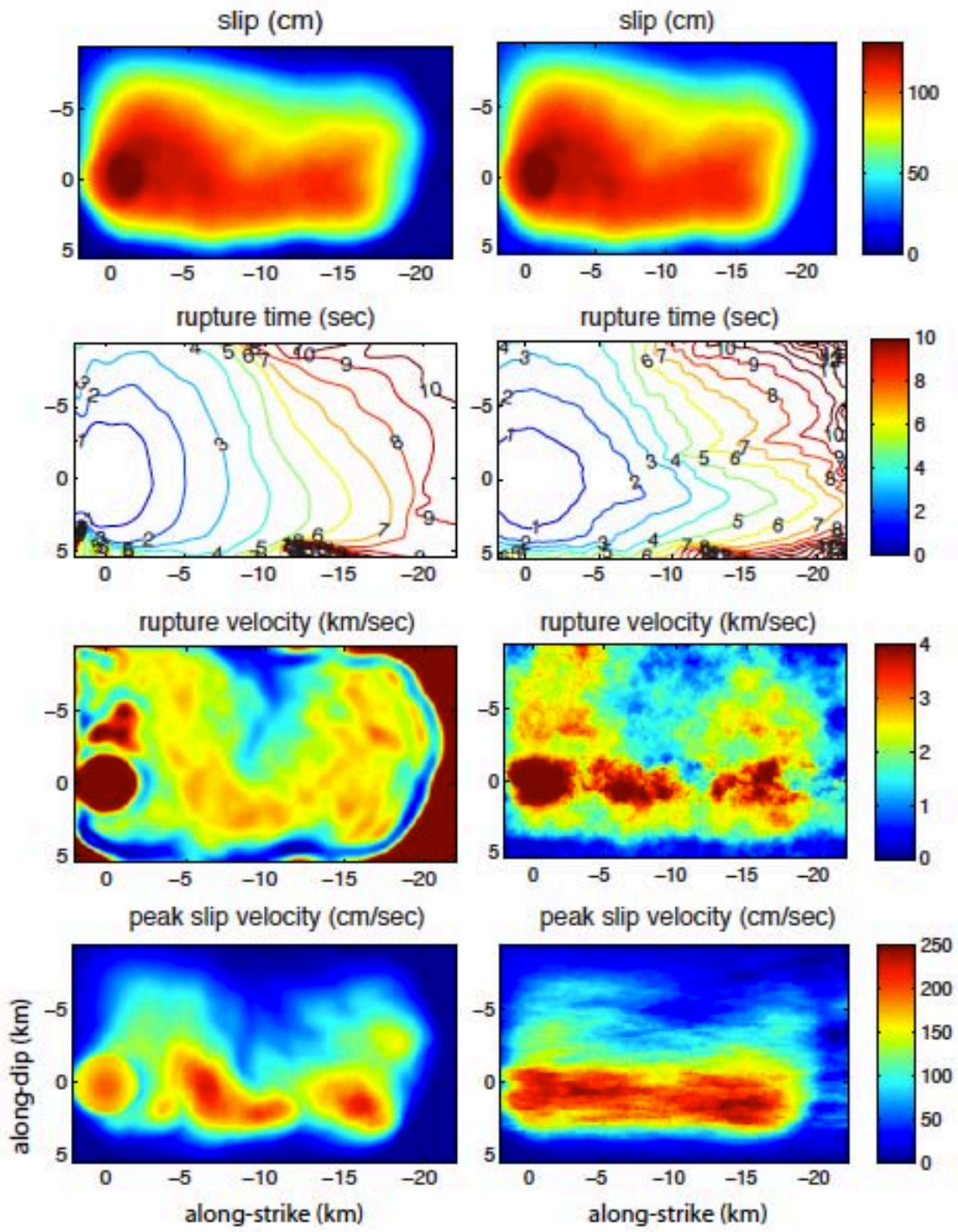

Figure 4. Pseudo-dynamic source modeling. (a) Source parameters obtained from the full dynamic modeling in Figure 2. (b) Source parameters obtained from the spatial random field model with 1-point and 2-point statistics extracted from the dynamic source model. In this modeling we only use mean, variance, and depth-dependency of the mean and variance for 1-point statistics and correlation length for 2-point statistics as a first order approximation. The Gaussian distribution is assumed for the 1-point statistics and the Exponential function is used for 2-point auto- and cross-correlations.

If relevant 1-point and 2-point statistics are extracted from the dynamic model, we can perform stochastic modeling to generate a large number of kinematic rupture models, but they all honor the target 1-point and 2-point statistics inferred from dynamic rupture models. Figure 4 shows an example of stochastic modeling, i.e., pseudo-dynamic modeling with a spatial random field model. The left panel shows the dynamically generated kinematic motions from Figure 2 while the right panel shows kinematic parameters generated by the pseudo-dynamic modeling. The same static slip distributions are used in both modeling approaches for comparison purposes. Since the objective of stochastic modeling is not to capture all the details of dynamically derived source processes in a deterministic way, the kinematic motions on the right panel are not supposed to be identical to ones on the left panel. But they are supposed to share the same pattern of 1-point and 2-point statistics. In particular, we can observe that the depth-dependency of kinematic parameters is well implemented in the right panel.

It is quite interesting to compare near-source ground motions generated by two different approaches (Figure 5). We also added an additional modeling approach for comparison purposes, i.e., pure kinematic modeling with the same static slip distribution, but constant temporal source parameters such as constant rupture velocity and constant peak slip velocity, etc. It is encouraging to see that the pseudo-dynamically generated source model produces ground motions (red traces in Figure 5b and 5c) quite consistent with dynamically generated ground motions (black traces) at least if stations are located in the middle of the surface projected area of a faulting plane. The pure kinematic modeling fails to do so (blue traces in Figure 5b and 5c). If stations are located above near the faulting boundary, both pseudo-dynamic and kinematic approaches fail to capture main characteristics of dynamically generated ground motions (Figure 5d), which implies that stopping phases may not be well implemented even in the pseudo-dynamic modeling.

If pseudo-dynamically generated source models can capture main characteristics of dynamically generated source models, this implies that we can simultaneously benefit from both computational efficiency in kinematic modeling and physical consistency from rupture dynamics in the framework of pseudo-dynamic source modeling. In addition, kinematic parameters are relatively well constrained by data compared to dynamic parameters. Thus better data constraints may be included in the pseudo-dynamic modeling. We believe that finite fault source modeling for simulating ground motions should target to fulfil at least three requirements. First they need to produce physically admissible models, which is the main concept of physics-based source modeling. As illustrated in Figure 6a, non-physical source models (red solid circle) need to be excluded by assigning zero probability. Secondly, we need to sample a full range of physically admissible potential events. This means that there should be no major holes, which are missed in the source modeling. For example, if we assume that one blue solid circle in Figure 6a indicates 100 rupture scenarios, so we have generated 300 physically admissible rupture scenarios. However, ground motion characteristics simulated by the 300 rupture scenarios may not contain ground motion characteristics from the 100 events represented by the blue open circle. If a next event occurs from a group of events covered by the blue open circle in Figure 6a, it will raise a serious issue in terms of simulation-based seismic hazard and risk analysis. Lastly it would

be very beneficial if we can assign non-uniform probabilities in the range of physically admissible rupture scenarios as in Figure 6b.

The pseudo-dynamic source modeling in the framework of a spatial random field model with dynamic rupture models generated for the Visp area provides a great opportunity to test the efficiency of a new pseudo-dynamic source modeling approach (Song and Somerville, 2010) and to complement dynamically generated ground motions with pseudo-dynamic modeling for simulation-based ground motion predictions in the Visp area.

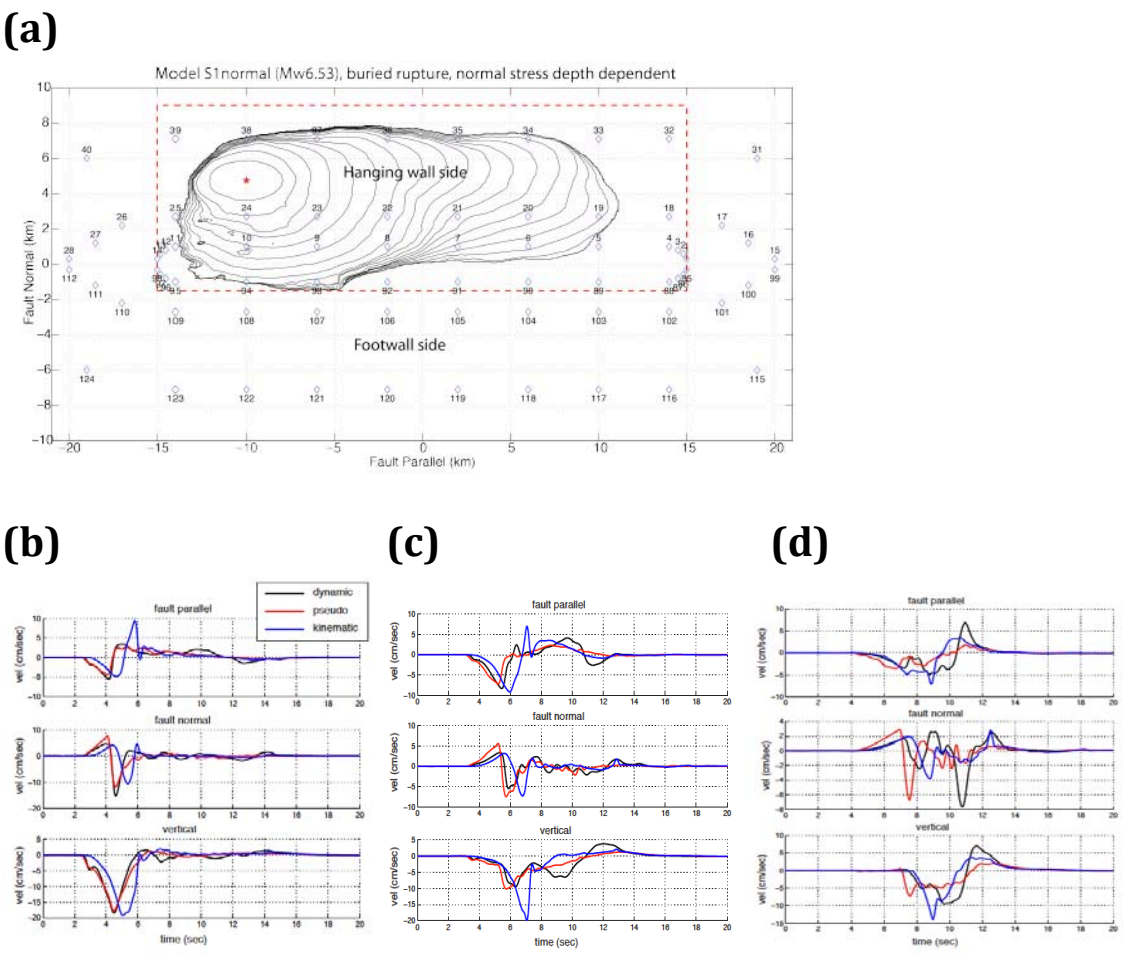

Figure 5. Synthetic ground motions from three different source modeling approaches: full dynamic (black), full kinematic (blue), and pseudo-dynamic (red). (a) Station locations with a finite faulting plane projected on the surface. Ground motions are compared in (b), (c), and (d). The pseudo-dynamic modeling produces ground motions consistent with the full dynamic modeling in (b) and (c).

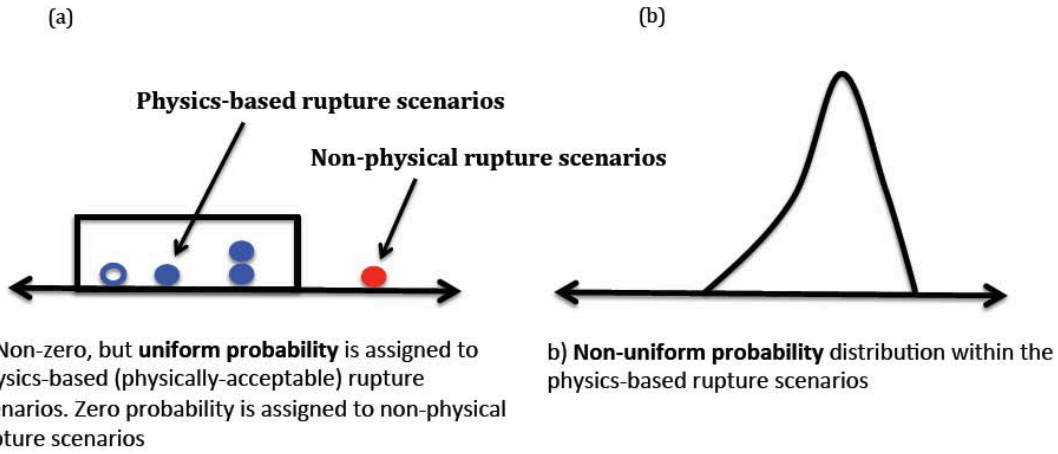

Figure 6. Schematic diagram that explains the concept of efficient finite fault source modeling with probability distributions. Physics-based (or pseudo-dynamic) rupture modeling may help us to exclude non-physical rupture scenarios, but this concept of source modeling does not necessarily imply that we quantify the likelihood of physically admissible rupture scenarios and sample them appropriately.

References

Dalguer, L.A. (2011). Rupture dynamics and resulted ground motion data of 360 earthquake models.

Guatteri, M., P. M. Mai, G. C. Beroza (2004). A pseudo-dynamic approximation to dynamic rupture models for strong ground motion prediction, Bull. Seism. Soc. Am. 94, 2,051-2,063.

Mena, B., L.A. Dalguer, and P.M. Mai (2012). Pseudo dynamic source characterization for strike-slip faulting, including stress heterogeneity and super-shear ruptures, Bull. Seism. Soc. Am., in press.

Schmedes, J., R. J. Archuleta, and D. Lavallée (2010). Correlation of earthquake source parameters inferred from dynamic rupture simulations, J. Geophys. Res., 115, B03304, doi:10.1029/2009JB006689.

Song, S., A. Pitarka, and P. Somerville (2009). Exploring spatial coherence between earthquake source parameters, *Bull. Seism. Soc. Am.* 99, 2,564-2,571.

Song, S., P. Somerville (2010). Physics-based earthquake source characterization and modeling with Geostatistics, *Bull. Seism. Soc. Am.* 100, 482-496.

Dynamic rupture models and ground motion simulations

Cyrill Baumann

III MODELLING OF EARTHQUAKE SCENARIOS IN VALAIS

3.1 INGREDIENTS FOR EARTHQUAKE MODELLING

Computer Code

Our research group possesses one of the worldwide most accurate and efficient open-source code to develop research on the field of earthquake source dynamics. This is the Support Operator Rupture Dynamics code (SORD). The SORD code developed by (Ely, Day et al. 2008) was implemented using a generalized Finite Difference scheme that can utilize meshes of arbitrary structure and incorporate irregular geometry, with the capability to model general fault geometry and topography. The technique deploys the method of Support-Operators (SOM) developed by (Samarskii 1982) and (Shashkov 1996). SOM is a general scheme for discretizing the differential form of partial differential equations.

The SORD solves the three-dimensional visco-elasto-dynamic equations of motion. The scheme is explicit in time, and uses a hexahedral, logically rectangular mesh. The artificial boundaries at the computational domain have absorbing boundary condition, to suppress artificial wave reflections, using Perfectly Matched Layers (PML). The wave propagation accuracy of this approach was tested using a layered material model in a highly deformed mesh, showing good agreement with the frequency-wavenumber method.

To model dynamic rupture propagation, the method uses the split-node technique for the fault boundary condition e.g. (Dalguer and Day 2007). The method is generalized for non-planar fault, allowing also for fault opening. The dynamic rupture occurs as dictated by the local stress conditions and a frictional failure law. At present, the slip-weakening friction model is implemented. The code is parallelized, using Message Passing Interface (MPI), for multiprocessor execution, and is highly scalable, enabling large-scale earthquake simulations. The dynamic rupture model has been validated through the Southern California Earthquake Centre (SCEC) dynamic rupture code validation exercise, showing good agreement with semi-analytical boundary integral methods (Harris, Barall et al. 2009). The resolution of the models is dx=dy=dz=0.1Km. The calculation is performed at Rosa, a Cray XT5 computer at the Swiss National Supercomputing Center (CSCS) in Manno, using 4096 processors.

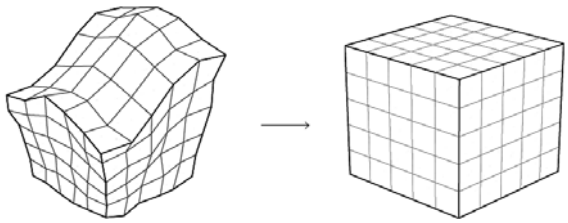

Figure 15: Map of Cartesian to logical space (Ely, Day et al. 2008)

SORD solves the three dimensional visco-elasto-dynamic equation of motion (2) & (3) coupled to frictional sliding, expressed in the fault boundary conditions (4.1 & 4.2).

$$\rho \dot{v}_i = \partial_i \sigma_{ij} \qquad (2)$$

with Hooke's law

$$\dot{\sigma}_{ij} = C_{ijpq} \partial_p v_q + \eta \dot{v}_q \qquad (3)$$

and the fault boundary conditions

$$\tau - \tau_c \leq 0 \qquad (4.1)$$

$$\vec{\tau}\dot{s} - \tau_c \dot{\vec{s}} = 0 \qquad (4.2)$$

(2) displays the stress-velocity formulation of the equation of motion with the density ρ, velocity v and stress tensor σ. Equation (3) shows Hooke's law with the viscosity η and the elastic tensor C. In equation (4), τ_c is the frictional strength of the fault. Frictional strength can generally be a function of many factors (e.g. normal stress, slip, slip rate, state variables). (4.1) states that shear stress τ can never exceed frictional strength, (4.2) states that slip is always directed opposit to frictional resistance. In our models, a running shear crack is propagating and forming the rupture.

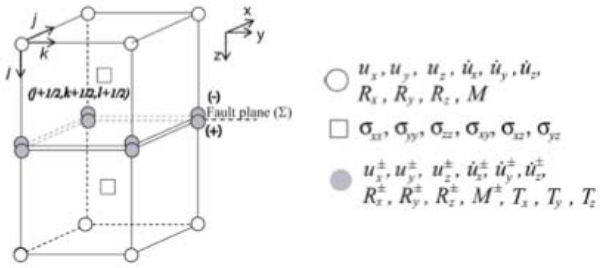

Figure 16: Partially staggered grid. We use split-node at the fault discontinuity. *R* signs restoring force, the elastic contribution from the deforming grid and *T* is traction on the fault.

The discrete representation of the equation of motion in the partially staggered grid (Day 1982) has the following form

$$\dot{u}_i^{(\pm)}(t + \Delta t/2) = \left(\frac{R_i^{(\pm)}}{M^{(\pm)}} \mp \frac{A}{M^{(\pm)}} T_i\right)\Delta t + \dot{u}_i^{(\pm)}(t - \Delta t/2) \qquad (5)$$

With equation (5), it is possible to calculate the future velocity on the positive and the negative side of the fault-discontinuity $\dot{u}_i^{(\pm)}(t + \Delta t/2)$. R are the restoring forces, M the mass term, A grid area, Δt time step and T traction term. The slip rate is simply expressed by

$$\dot{s}_i = u_i^{(+)}(t + \Delta t/2) - u_i^{(-)}(t + \Delta t/2) \qquad (6)$$

The index is standing for the planar components i=x,y and the traction is calculated as followed: $T_i = T_{current} - T_{initial}$.

The SORD code solves the equation of motion and assumes then the slip rate (6) to be zero. Substituting equation (5) into equation (6) and solving for the traction term, we obtain a trial traction value, which then is evaluated: If the trial traction is below a certain critical value $T_{trial} < T_{critical}$, the assumption, slip rate is equals to zero, was correct. But if the trial traction is equal or exceeds a critical stress value, $T_{trial} \geq T_{critical}$, the assumption of zero slip rate was wrong. In that case, the traction evolves according to a specified friction law (in our case: linear slip weakening law).

Initial Stresses on the Fault

Testing a variety of auto-correlation functions to fit the spectral properties of a large number of slip distributions, one observes that a von Karman auto-correlation function with magnitude-dependent correlation lengths and a scale-invariant Hurst-number best maches the slip heterogeneity spectra (Mai and Beroza 2002).

$$P(k) = \frac{\sigma^2 \left(2\sqrt{\pi}a\right)^3 \Gamma\left(\nu + \frac{3}{2}\right)}{\Gamma(\nu)\left(1 + k^2 a^2\right)^{\left(\nu + \frac{3}{2}\right)}} \qquad (7)$$

Equation (7) is the three-dimensional von Karman autocorrelation function in Fourier domain. σ the standard deviation, a correlation length, the largest scale for which the scaling is described by a power law, the Gamma function Γ, wave number k and Hurst exponent v. For structures smaller than the correlation length, stress distribution is behaving fractally. In our models, we defined a correlation length along strike (in most of experiments 20.0m, in some few experiments 8m), along dip (8m) and a Hurst exponent (in most experiments 0.001, in some few ones 0.5).

Initially, we defined a plane with dimensions corresponding to the expected moment magnitude (around Mw=6.5). For this plane, we generated stochastic stress according to a von Karman distribution. The area outside of the plane has such a high coefficient of friction, that rupture cannot appear there. A representative example of a stress distribution prior to the earthquake is given in Figure 17.

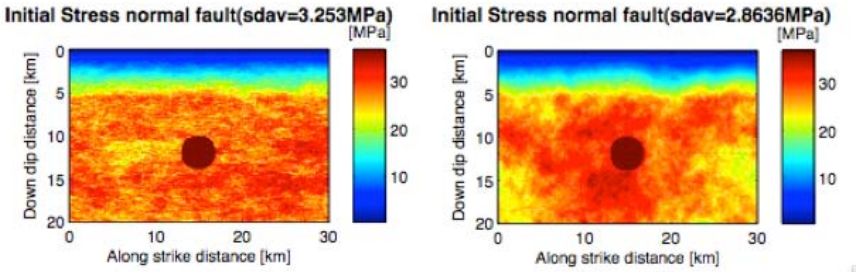

Figure 17: Initial shear stress von Karman distribution. At the surface, shear stress vanishes (free-surface condition). The redish circle in the centre is the nucleation patch with a radius of about 2 Km. *Left*: Hurst exponent of about 0.001. *Right*: Hurst exponent of about 0.5 – the larger the Hurst exponent, the smoother the stress distribution.

In most of the models we use a normal stress depth-dependence down to 5 Km along dip. In larger depths, normal stress is assumed to be constant. A few models assume a normal stress depth dependence along the entire dip down to 20 Km depth. This is shown in Figure 18.

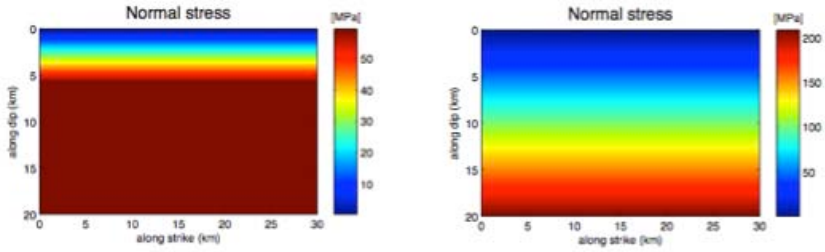

Figure 18: Normal stress distribution with a depth-dependence along dip down to 5 Km (left) and 20 Km (right). Normal stress vanishes at the surface (free-surface condition).

Rock Properties

We use a one-dimensional rock-velocity-model for Alpine regions according to Diel et al. 2005 (AG Seismologie, Stuttgart). They inverted 277 events (P-waves) and 283 events (S-waves) in the area of Switzerland to obtain the minimum-1D-model for P- and S-waves for Alpine regions. Within the first 2 Km we assume a gradient model (Figure 19, right). Figure 20 shows the density model which is fairly simple.

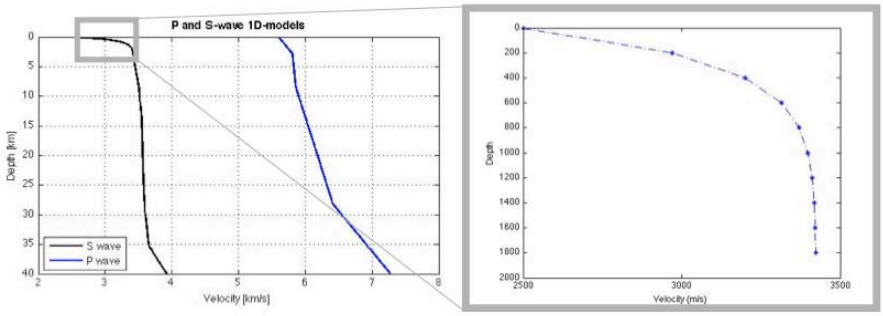

Figure 19: 1D-minimum model for P- and S-waves in Alpine regions according to Diehl et al. 2005. For the first 2 Km, we use a simple gradient-model (Poggi 2010, personal communication).

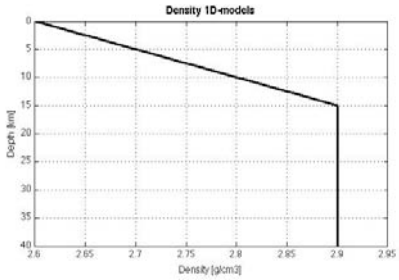

Figure 20: Density model: Down to 15 Km depth along dip, the density is linearly increasing. In depths larger than 15 Km, the density is constant 2.9g/cm^3.

Fault Mechanism and Geometry

Section II already revealed that it makes sense to model strike-slip and normal faults in order to generate earthquake models in the region of Visp. Regarding to normal faults, we modeled a dip of about 45°, which will be explained in *Section 3.4.2*, where we investigate the impact of dip on magnitude and ground motions. The fault has dimensions of about 30x20 Km.

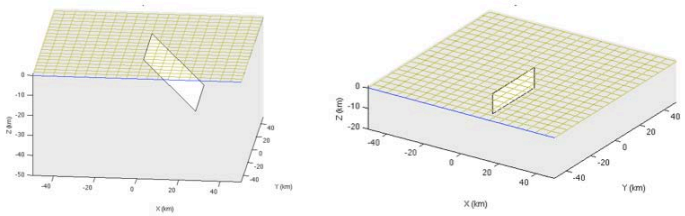

Figure 21: *Left*: normal fault diping 45°. *Right*: strike-slip fault.

Fracture Criterion

We use a linear slip-weakening law (Andrews 1976), where the coefficient of friction *f(l)* a function of slip *l* is. Frictional strength is assumed to be proportional to normal stress: $\tau_c = -f(l)\sigma_n$. If slip is smaller than a critical slip distance D_c, static coefficient of friction is reduced. If slip is equal or larger than the critical slip distance, static coefficient of friction drops to dynamic coefficient of friction (8).

$$f(l) = \begin{cases} f_{static} - \left(f_{static} - f_{dynamic}\right) l / D_c & l < D_c \\ f_{dynamic} & l \geq D_c \end{cases} \qquad (8)$$

Linear slip-weakening is widely spread in the computational seismology community and simple to implement in a code. Many rupture related features can be explained with this law. Disadvantages of

the slip-weakening law are, that it does not account for thermal effects (thermal pressurization, flash heating), it does not account for healing effect, and it is not dependent on sliding velocity, which was shown in laboratory experiments (Marone 1998).

Empirical Scaling Relationships

In order to see if our models behave well at the source, we expanded the model space and generated earthquake models with magnitudes larger than the expected magnitude in the region of interest - Visp. The goal was to compare earthquake model data over a wide magnitude-range with empirical relationships. We compared our data with empirical relationships of (Wells and Coppersmith 1994), (Somerville, Irikura et al. 1999) and (Mai and Beroza 2000). Figure 22 shows rupture area as a function of moment magnitude. Model data (blue dots) fit quite well all three empirical relationships. Model data fit also the empirical relationships between moment magnitude and mean slip (Appendix A1).

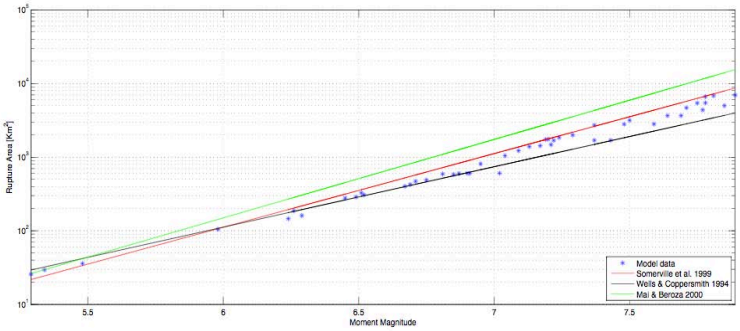

Figure 22: Comparison of model data with empirical relationships of (Wells and Coppersmith 1994), (Somerville, Irikura et al. 1999) and (Mai and Beroza 2000). Model data (blue dots) fit empirical relationships quite well.

3.2 WHAT INITIAL CONDITIONS DETERMINE THE MAGNITUDE OF AN EARTHQUAKE

We modeled surface-breaking normal-faulting earthquake scenarios with moment magnitudes Mw = 5.51-7.02 using a model domain with dimensions of about 102.3x51.5x239.8 Km and a fault size of 30x20 Km (Figure 23).

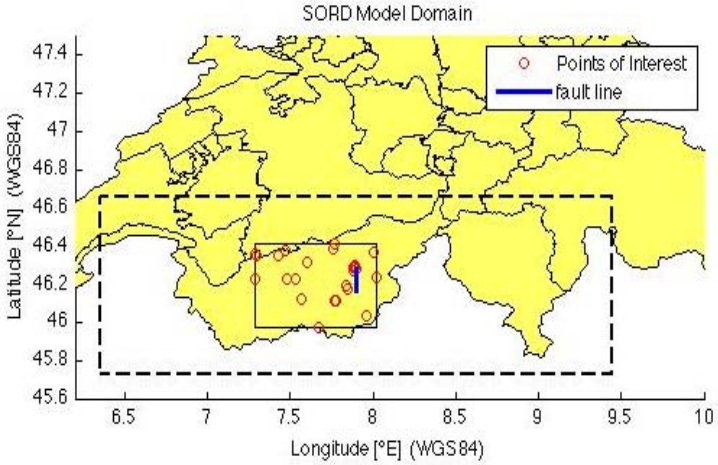

Figure 23: Map showing Switzerland (yellow) and the model domain (black dashed line). The blue line shows the fault outcrop in the valley of Visp. Red dots show seismic stations of special interest (near fire stations etc.). Fine black solid line narrows area containing all points of interests.

Model	Mechanism / Dip [°]	Remarks	Moment Magnitude
45m10normal			*5.51*

45m11normal	Normal Faulting, 45°		*5.57*
45m12normal			*5.51*
45m13normal			*6.02*
45m69normal			6.24
45m70normal			6.91
45m71normal			6.87
45m72normal			7.02
45m73normal			6.81
45m74normal			6.90
30m86normal	Normal Faulting, 30°	all have the same initial setting	6.90
40m87normal	Normal Faulting, 40°		6.90
60m88normal	Normal Faulting, 60°		6.90
80m89normal	Normal Faulting, 80°		6.93
70m91normal	Normal Faulting, 70°		6.91
50m92normal	Normal Faulting, 50°		6.90
35m93normal	Normal Faulting, 35°		6.90
45m94normal	Normal Faulting, 45°		6.90
88m95normal	Normal Faulting, 88°		6.95

Table 1: Overview of Visp-models. If there is no remark, the corresponding run has its own initial settings.

A list of all earthquake models performed in order to evaluate ground motions is shown in Table 1. There are 2 groups of earthquake models with a dip of 45°: group 1 with 5.51≤Mw≤6.02 and a group with larger magnitudes 6.24≤Mw≤7.02. The question arises, what determines the magnitude of an earthquake. One aspect is certainly the size of the area where the rupture can propagate. In all our models, the size of the potential fault was exactly the same: 30x20Km. Therefore, additional factors determined the magnitude.

Considering the initial parameters of earthquakes with magnitudes Mw = 6.02 and smaller and earthquakes with magnitudes Mw = 6.24 and larger, we list the differing parameters in Table 2 (a list of all other parameters is given in the Appendix A6).

Parameter	Models with Mw≥6.24	Models with Mw≤6.02
static coefficient of friction [1]	0.60	0.62
dynamic coefficient of friction	0.40	0.55
critical slip distance	0.20 m	0.30 m
critical slip distance at nucleation	0.20 m	0.30 m
normal stress depth dependence down to	4 Km	20 Km
overshoot	1.5	1.65
correlation length along strike	20 Km	8 Km
Hurst exponent	0.001	0.5

Table 2: Differing initial parameters of low-magnitude earthquakes (Mw≤6.02) and large-magnitude earthquakes (Mw≥6.24). All other parameters were in both model series identical.

We performed additional experiments to evaluate what influences the magnitude of an earthquake. The basic framework of those numerical runs was formed by parameters given in Table 2 (left column). Models with those parameters had an average moment magnitude of Mw=6.8811±0.0615 (45m70normal-40m74normal) and models with parameters according to Table 2 (right column) produced an average moment magnitude of Mw=5.77±0.3386 (45m10normal-45m13normal) which is about 1 magnitude lower.

[1] typical range of rock friction coefficients ($0.6<\mu_s<0.85$), Byerlee, J. (1978). "Friction of rocks." Pure and applied geophysics **116**(4): 615-626.

We performed new runs by applying the initial settings corresponding to Table 2 left column and changed only one or two parameters (see Table 3). The depth dependence was in all models (45m80normal – 45m85normal) down to 4Km.

Model	New Parameters	Remarks	Mw
45m80normal	-Hurst exponent H = 0.5	All other parameters according to Table 2, left column	7.05
45m81normal	-correlation length along strike acx = 8Km		6.93
45m82normal	-overshoot = 1.65		6.51
45m83normal	-static coefficient of friction mus = 0.62 -dynamic coefficient of friction mud = 0.55		5.41
45m84normal	-according to Table 3, right		4.63
45m85normal	-static coefficient of friction mus = 0.62 -dynamic coefficient of friction mud = 0.55 -Hurst exponent = 0.5	All other parameters according to Table 2, left column	6.39

Table 3: New runs and parameters that were used. Moment magnitude is shown in the last column.

Table 3 shows that Hurst exponent and correlation length along strike respectively do not change the magnitude of our models significantly. Much larger impacts have overshooting and particulary the difference between static and dynamic coefficient of friction (stress drop). If static and dynamic coefficient of friction are close together, stress drop will be small too. Parameters in Table 2 (right) provide the smallest magnitude.

3.3 REPRESENTATIVE MODEL

As a representative example we show here 45m80normal – a normal faulting model with a dip of 45°. Initial parameters are shown in Table 3 (Section 3.2). Particulary in 45m80normal we used a Hurst exponent of 0.5 instead of 0.001 which we used usually.

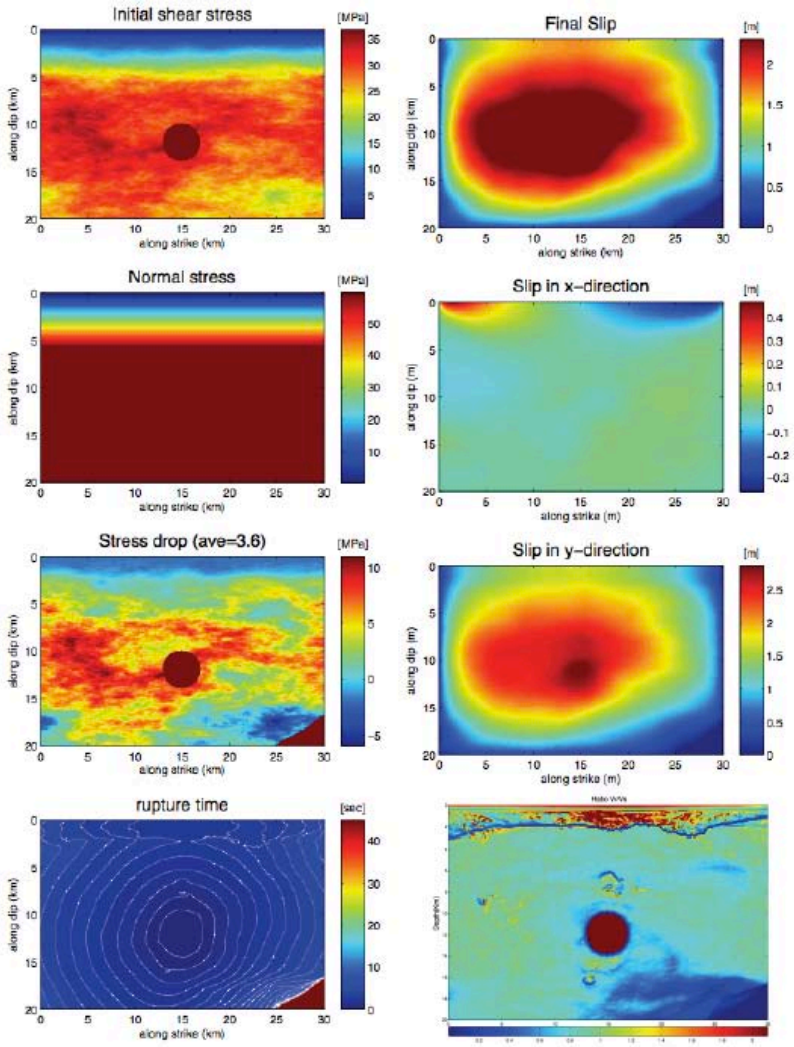

Figure 24: Overview of model 45m80normal data: initial shear stress, normal stress, stress drop, rupture propagation, final slip, slip in x- and y-direction and supershear distribution.

Initial normal- and particulary shear stress determines the rupture propagation. Looking at the initial shear stress: in the bottom right corner initial shear stress is lowered compared to the rest of the fault. Stress drop and rupture propagation show that this area with lowered initial shear stress prevents rupture to propagate there. Apart from that rupture is propagating almost circular, mainly because of the regular distribution of large initial shear stress (>30MPa).

Because of the normal faulting mechanism, there is almost no slip in x-direction (along strike). Main slip is directed in y-direction.

Figure 24 bottom right shows the distribution of supershear rupture velocity. Plotted is the ratio between rupture velocity and shear wave velocity. If that ratio exceeds one, rupture is propagating with supershear velocity. Supershear is mainly localized at the surface.

3.4 COMPARISON WITH GROUND MOTION PREDICTING EQUATIONS

3.4.1 VALIDITY OF EARTHQUAKE MODELS IN ALPINE REGIONS REGARDING TO MAGNITUDE AND GROUND MOTION PARAMETERS

It is well known that current ground motion predicting equations (GMPE) are insufficent to predict near-source ground motion. The reason is that GMPE are based solely on recorded data which are

sparse in the nearfield. Therefore, physics-based numerical models are required if we are to adequately assess the level and variability of near-source ground motion.

Definition of Peak Values

Before we consider ground motion parameters, we need to define what the peak values are, for example peak ground velocity (PGV). How do we measure a peak value? In our study, we used maximum horizontal component (9.1) and the geometric mean of the two horizontal components (9.2), defined in case of PGV as followed.

$$h = \max\left\{PGV_x, PGV_y\right\} \qquad gm = \sqrt{PGV_x \cdot PGV_y}$$

The same definition can be applied for Peak Ground Displacement (PGD) and with Peak Ground Acceleration (PGA) as well as for Spectral Acceleration (SA).

The geometric mean exhibits an important disadvantage which can be illustrated on the base of strike-slip mechanism.

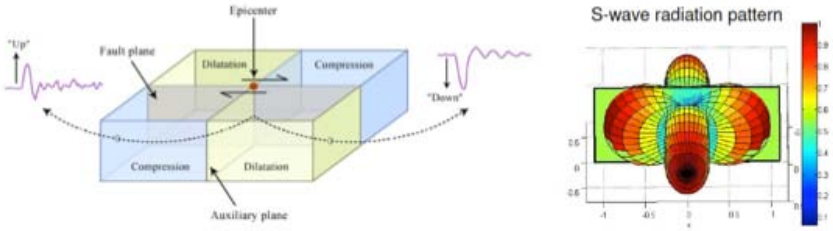

Figure 25: *Left*: strike-slip fault showing compressional and dilatational parts of the rupture as well as the nodal and auxilary plane. *Right*: S-wave radiation pattern an nodal plane. The radiation on the nodal plane vanishes (M. Kaeser).

Ground motions in the near-field are dominated by P- and S-waves. The S-wave radiation as well as the P-wave radiation vanishes at the nodal plane. Assuming we measure the geometric mean of the maximum horizontal value in x- and the maximum horizontal value in y-direction. Near a nodal point or plane, one of the horizontal components can be a near-zero value while the other horizontal component is not. This would lead to a geometric mean which is near zero. In case of the maximum horizontal component, the larger value would be taken to be the peak value.

(Ripperger, Mai et al. 2008) investigated the variability of near-field ground motion from dynamic earthquake rupture simulations in case of a strike-slip fault. They compared geometric mean of the two horizontal components with a definition called GMRotD50. Figure 26 shows that a low fault parallel (a) and a high fault normal (b) component lead to a low geometric mean (c) while GMRotD50 (d) does not exhibit low values.

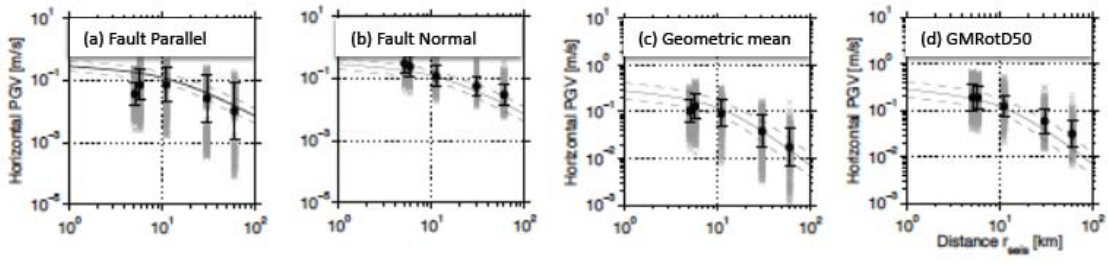

Figure 26: Study about different peak ground velocity definitions (Ripperger et al. 2008). Shown is the variability of near-field ground motion from dynamic earthquake rupture simulations in case of a strike-slip fault mechanism. (a) shows fault parallel, (b) fault normal component, (c) geometric mean and (d) orientation-independent measure GMRotD50.

GMRotD50 is an orientation-independent measure. In some GMPE GMRotD50 is applied e.g. (Boore and Atkinson 2008) because it is a way to calculate a geometric mean without having an impact of stations near the nodal plane. How is it calculated? In a first step, the two orthogonal (horizontal) components are rotated from 1—90° in 1°-steps. The evaluation of the simple geometric mean is performed for each pair of rotated time series. The final measure is the median value of all geometric means. In our numerical runs, we compare maximum horizontal component with geometric mean.

Definition of Distance

Besides the definiton of peak value, the question arises how we define the distance of a seismic station to the rupture fault. We particulary considered two kind of definitions: first, the Joyner-Boore distance (JB), which is defined as the shortest distance between the seismic station and the surface projection of the fault. Second, the rupture distance (DistRup), which is the shortest distance between the seismic station and the rupture fault. Some GMPE use Joyner-Boore distances, some use rupture distances and some use other definitions of distance.

S-Wave-Velocity Correction

A further issue of our models represents the high S-wave velocities within the first 30m depth. Section 3.1 shows that the initial S-wave velocity is 2500 m/s. This value seems to be too high, because in fact, rock is usually covered by sediments, especially in the Rhone and Visp valley that are filled with alluvial sediments. Those sediments lead to S-wave velocity reductions down to about 1500m/s and less at the surface. To account for this, we applied a period-dependent site amplification (deamplification) correction according to (Borcherdt 1994) in which we reduced the velocity within the first 30m to 1500m/s.

Ground Motion Predicting Equations (GMPE's)

We compare our model data with two different ground motion predicting equations: (Boore and Atkinson 2008) (BA08) and (Akkar and Bommer 2010) (AB10). AB10 has a moment magnitude range of Mw=5.0-7.6, and data (PGA, PGV, PSA) up to a distance of 99 Km. The range of period is T=0.05-3.0s. BA08 has a larger moment magnitude range: Mw=5.0-8.0, provides data (PGA, PGV, PSA) to larger distances (200 Km) and has a larger period range: T=0.01-10s. Both, AK10 and BA08, use JB distances. BA08 can be applied worldwide, whereas AB10 is particulary for Europe and middle east. BA08 uses GMRotD50, AK10 uses geometric mean. Both GMPE are widely spread in the community.

Misfit-Function and Results

In a first step, we evaluated which definition of peak value and fault distance is appropriate in order to gain a maximum fit with GMPE. We compare maximum horizontal component with geometric mean of the two horizontal components. Furtermore we compare Joyner-Boore distance with rupture distance. In order to measure the deviation from the GMPE, we used the following misfit function (Cabrera 2010):

$$\sum_{res} = \frac{\sum_{i=1}^{N}(obs_i - sim_i)^2}{\sqrt{\sum_{i=1}^{N} obs_i^2}\sqrt{\sum_{i=1}^{N} sim_i^2}} \qquad (10)$$

with *obs* values given by GMPE's and *sim* data taken from the models. The larger the misfit, the larger the deviation from the GMPE.

Figure 27 and 28 show the results. For each earthquake scenario one can see synthetic data points compared with ground motion predicting equations (BA08 in blue and AB10 in red) taken once the geometric mean of the two horizontal components and once the maximum horizontal component. In Figure 27 and 28 we used Joyner-Boore distances. Black numbers are misfit values according to equation (10). At the bottom one can see colored contour plots of rupture propagation, the moment magnitude and in brackets the model number. In Figure 28 spectral acceleration at a period of T=1s is plotted. Green dots are synthetic data points.

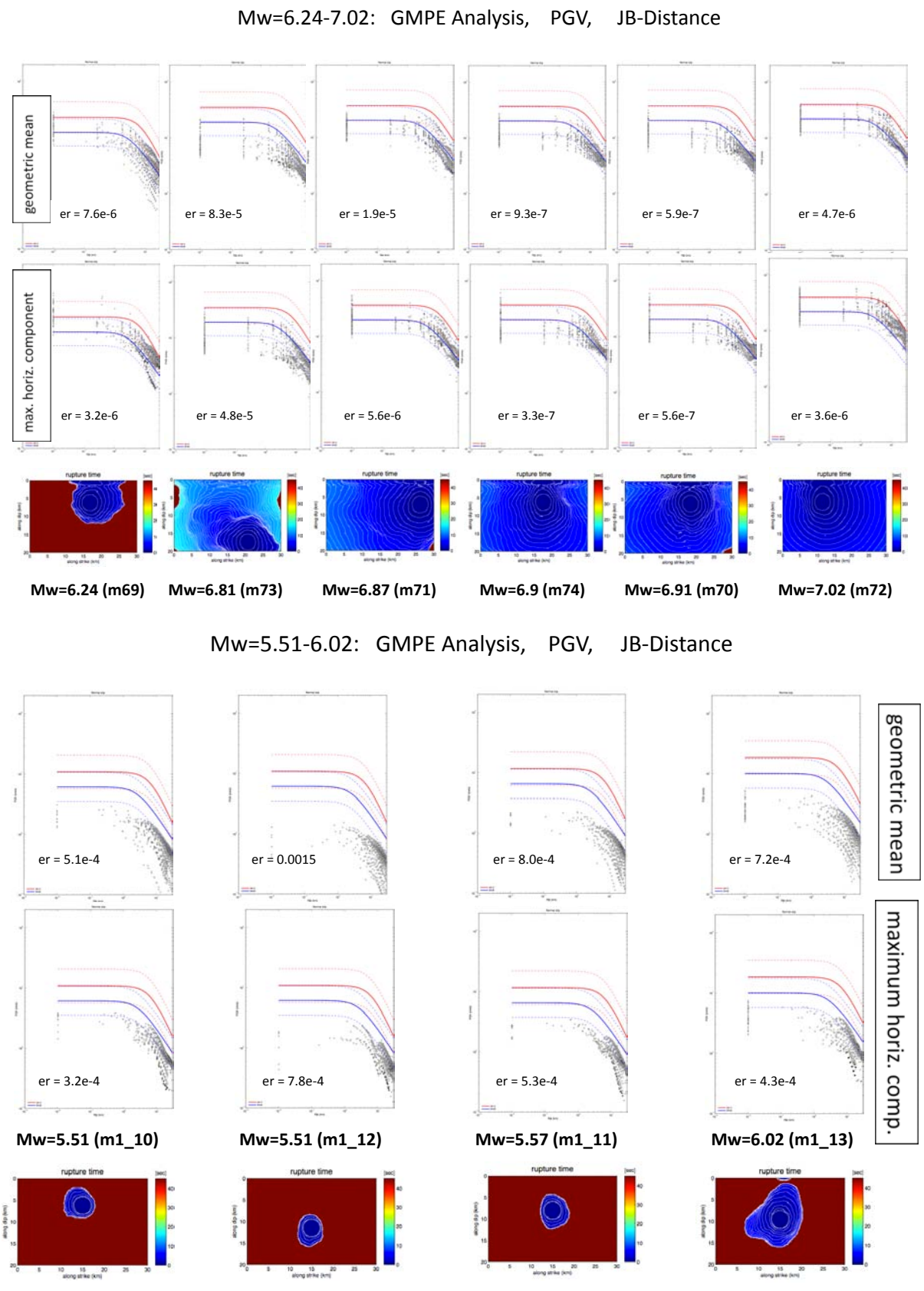

Figure 27: Synthetic peak ground velocity data points (black dots) compared with ground motion predicting equations of Boore & Atkinson (blue) and Akkar and Bommar (red). Used are Joyner-Boore distances. We compare geometric mean of horizontal components with maximum of horizontal components as definitions of peak values. Black numbers are errors according to misfit function (10). On bottom, there are contour plots of rupture propagation and the corresponding model (brackets) with moment magnitude. The fault mechanism is normal faulting.

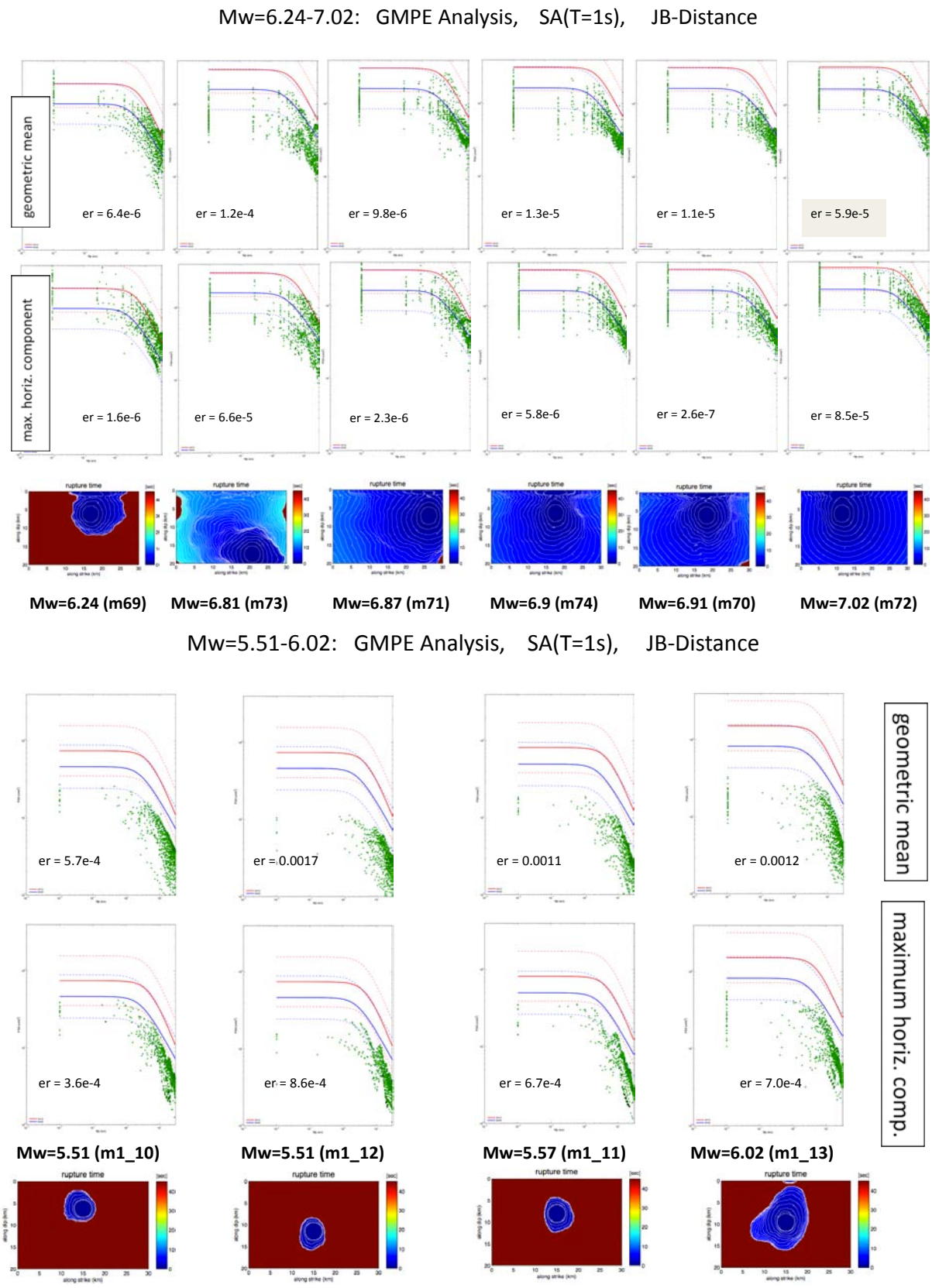

Figure 28: Synthetic spectral acceleration data points (green dots) at T=1s compared with ground motion predicting equations of Boore & Atkinson (blue) and Akkar and Bommar (red). Used are Joyner-Boore distances. We compare geometric mean of horizontal components with maximum of horizontal components as definitions of peak values. Black numbers are errors according to misfit function (10). On bottom, there are contour plots of rupture propagation and the corresponding model (brackets) with moment magnitude. The fault mechanism is normal faulting.

Figure 27 and 28 show that synthetic data (peak ground velocity and spectral acceleration at T=1s) generally better fit GMPE of BA08. This is perhaps because BA08 is more apropriate with respect to crustal active zones. It is also apparent, that the larger the moment magnitude is, the better the fitting with BA08 appears. There is a distinct step between earthquake models with magnitudes 5.51-6.02 and earthquake models with magnitudes 6.24-7.02. Figure 29 summarizes the insights of Figure 27 and 28. We performed exactly the same experiments with rupture distance (DistRup) instead of Joyner-Boore distances and we could observe the same features (see Appendix A2 & A3).

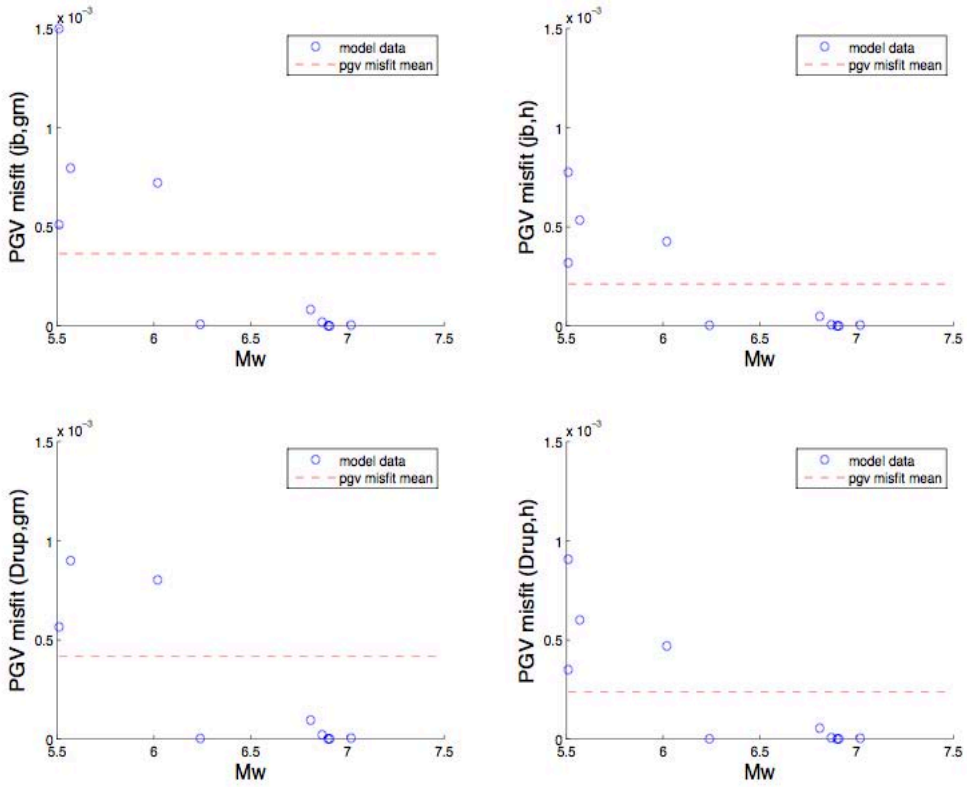

Figure 29: Result summary of comparison with ground motion predicting equations (PGV) of BA08. Blue dots are models (10 models with magnitudes Mw=5.51-7.02). Red dashed line displays the mean misfit. On the axis of abscissas, the moment magnitude is plotted, on the ordinate PGV misfit is plotted. *Top left*: JB distance, geometric mean. *Top right*: JB distance, maximum horizontal component. *Bottom left*: DistRup, geometric mean. *Bottom right*: DistRup, maximum horizontal component.

Figure 29 shows two groups of models: group one with models of moment magnitude 5.51-6.02 and group two with models of moment magnitude 6.24-7.02. The misfit, that means the deviation of synthetic PGV values from GMPE according to Boore and Atkinson 2008, is unreasonable high in group one compared to group two. This result shows that only models with magnitudes 6.24 and larger should be considered if we investigate ground motion parameters. Earthquakes with small magnitudes (<6.24) probably almost only nucleate and do not generate enough propagating waves.

The comparison between Joyner-Boore and rupture distance as well as between maximum horizontal component and geometric mean of the two horizontal components shows that best fitting of synthetic peak ground velocities is achieved with GMPE of BA08, if we use definitions of Joyner-Boore (distance) and maximum horizontal component for peak values (Figure 29, top right). The same observation can be established for spectral acceleration at a period of T=1s (see Figure 30). BA08 uses GMRotD50. Our results show, that the maximum horizontal component is more apropriate than the simple geometric mean to compare our synthetic peak values with BA08. This is probably because of the orientation-dependance of the geometric mean.

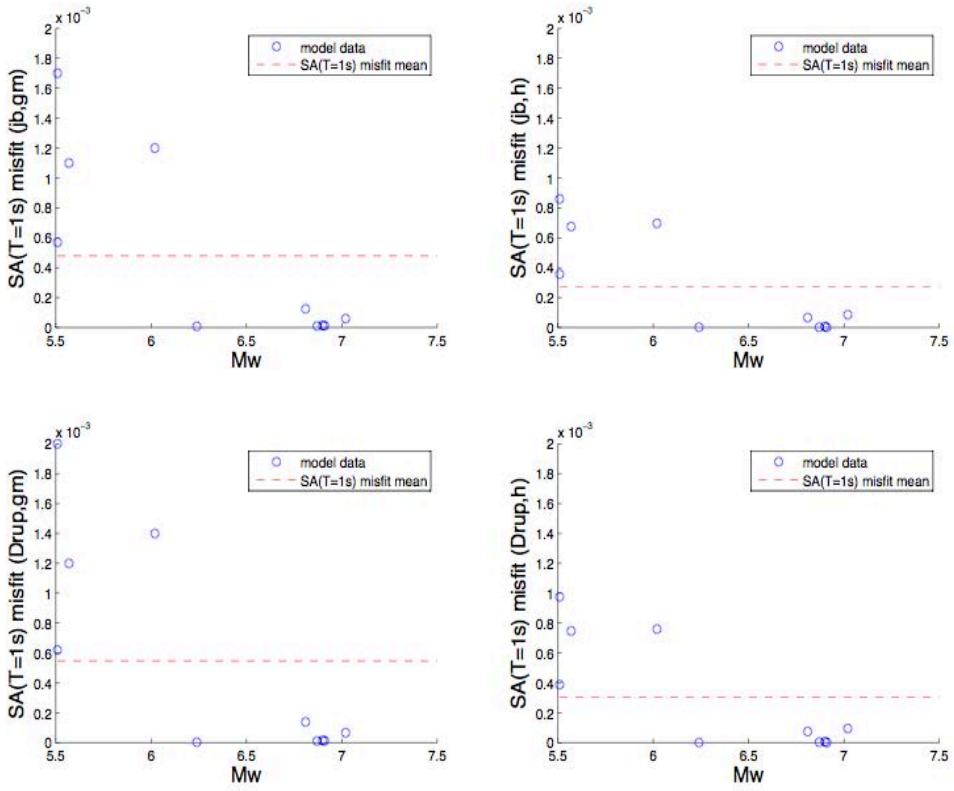

Figure 30: Result summary of comparison with ground motion predicting equations (SA, T=1s) of BA08. Blue dots are models (10 models with magnitudes Mw=5.51-7.02). Red dashed line displays the mean misfit. On the axis of abscissas, the moment magnitude is plotted, on the ordinate SA(T=1s) misfit is plotted. *Top left*: JB distance, geometric mean. *Top right*: JB distance, maximum horizontal component. *Bottom left*: DistRup, geometric mean. *Bottom right*: DistRup, maximum horizontal component.

For further ground motion parameter investigations, we used Joyner-Boore distances and the maximum of the two horizontal peak values in order to use BA08 as a reference.

Model Resolution and Spectral Acceleration: Appropriate Period Range

The previous considerations include also the evaluation of spectral acceleration at a specific period of T=1s. But is it more appropriate to compare synthetic data with GMPE at different periods? We calculated the misfit (Equation 10) between spectral acceleration and BA08 of 6 models with magnitudes 6.24 and higher at periods of 0.1, 0.2, 0.3, 0.4, 0.5, 0.6, 1.0, 2.0, 3.0, 4.0 and 5.0s, which is shown in Figure 31

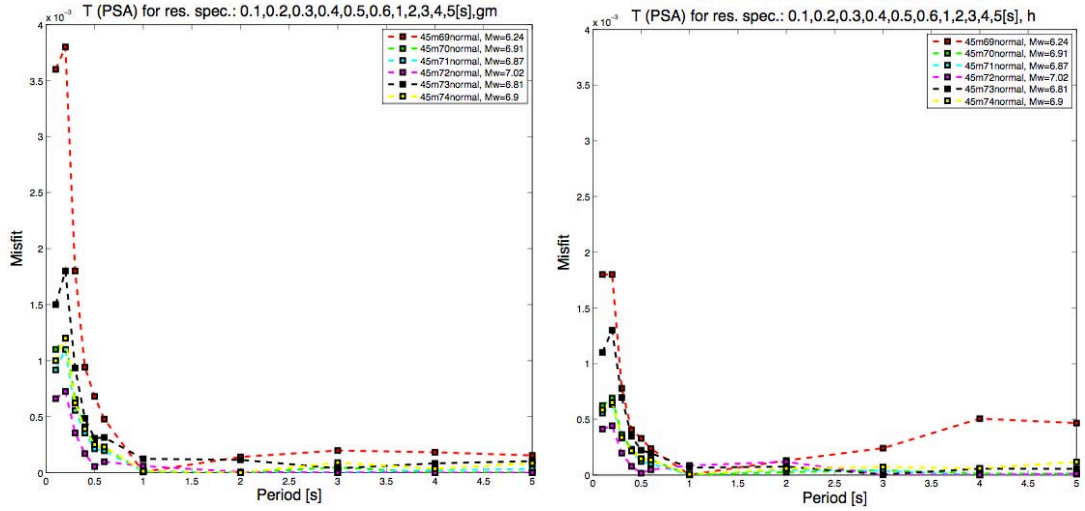

Figure 31 Misfit of spectral acceleration (deviation from GMPE BA08) as a function of Period for geometrical mean (*left*) and maximum horizontal component (*right*).

We compared geometric mean with maximum horizontal component. The average misfit of the selected models (45m69normal-45m74normal) was in case of geometric mean 7.711e-6. In case of the maximum horizontal component, the average misfit was lower: 2.4394e-6. The period where we had the best fitting for all models was independent of the definition of peak measure at T=1s. For periods less than 0.75s, the misfit is intolerably large and for periods larger than 0.75s, the misfit is generally around 6.67% of the maximum observed misfit and smaller.

Looking at the maximum horizontal component (Figure 31, right), there is one model, 45m69normal with Mw=6.24, that does not behave well: for periods larger than 2.5s, the misfit increases up to 29% of the maximum misfit of maximum horizontal component. So far the reason of that behaviour is not clear, perhaps the comparable small magnitude plays a certain role. But in fact, the model 45m69normal behaves well if we look at the geometric mean (Figure 31, left). Nevertheless, neglecting model 45m69normal, a general trend is visible: our models are behaving well for periods larger than 0.75s or frequencies smaller than 1.33Hz. Because we can only model low frequencies, it is not possible to generate peak ground accelerations (PGA) which are sensitive to high frequencies. Instead of PGA we use spectral acceleration.

In the method we use, the fault discontinuity is represented explicitly by incorporating discontinuity terms at velocity nodes in the grid which is called traction-at-split-node (TSN) method. The TSN is implemented in a scheme that employs second-order spatial differencing, which requires a minimum sampling of 10 grid points per wave length (Virieux 1986). The minimum resolvable wave length is therefore λ_{min}= 9•100m = 900m. The maximum resolvable frequency then is, assuming a minimum shear-wave velocity of 1500m/s (site-corrected), $f_{max} = v_{s,min}/\lambda_{min} \cong 1.67Hz$ which is similar to the 1.33Hz we obtained considering the spectral acceleration analysis.

We state that our models behave well for frequencies smaller than 1.33Hz. Usually for ingeneering interests, a frequency band up to 10Hz is considered, so we are modelling only the low-frequency part. For future work, there is the possibility to combine our finite-difference deterministic low-frequency wave simulations with statistical high frequency scattered waves to obtain broadband waveforms. In case of the New Zealand Christchurch Mw=6.3 earthquake 2011, pseudo-spectral acceleration at several stations exceeded gravity, in which extreme ground motion were observed in the low-frequency range of f = 1.0-2.5 Hz (T = 0.4-1.0s).

Misfit as a Function of Distance

An important question is how the misfit, the deviation of synthetic peak ground values from BA08, behaves as a function of distance. We evaluated models with Mw=5.51-7.02 as before. Generally, the misfit decreases with distance (independent of SA or PGV, independent of JB or DistRup, independent of maximum horizontal component or geometric mean). The decay is exponential and maximum misfit is at zero-distance. The misfit is reasonably small (<0.001 or 5% of the maximum misfit) for stations with distances larger than 15km. Generally, the larger the moment magnitude, the smaller the maximum misfit. Figure 32 shows some representative examples, the complete experimental series is put into the Appendix A4 & A5. We also compared maximum horizontal component with geometric mean and obtained the same results.

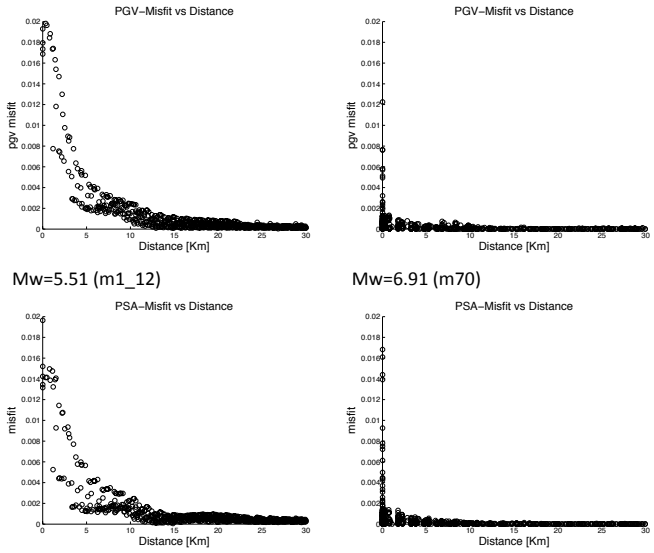

Figure 32: Deviation of synthetic peak values (PGV and SA(T=1s)) from BA01 (misfit) as a function of distance for 45m12normal and 45m70normal. Black circles are seismic stations. Distance is Joyner-Boore. We use here maximum horizontal component as the peak measurement. *Top row*: Peak Ground Velocity. *Bottom row*: Speactral Acceleration at T=1s.

3.4.2 IMPACT OF FAULT DIP ON MAGNITUDE AND GROUND MOTIONS

In our experiments we performed models with a dip of 45°. The question arises what was the motivation for choosing a dip of 45°. Several aspects play in this respect a role: the numerical aspect – if the mesh deformation, or in other words the dip, exceeds a certain value, the models become inaccurate. A second aspect is the question what provides nature? Which is the most frequent dip range for normal faults we can find in nature? As a third point, it is to evaluate how fault type, namely normal faulting, is realized in GMPE. Fourth, what is the impact of dip variation on moment magnitude and ground motions?

Evaluation of Dip-Impact Experiments

We performed several experiments to evaluate the impact of dip (Table 4). In those experiments we used a Hurst exponent of 0.5 and correlation lengths along stirke acx=8Km and along dip acy=8Km, because we think that a smoother initial shear stress distribution reflects nature in a more realistic way. For all models, we used the same setup (model domain with dimensions of about 102.3x51.5x239.8 Km and a fault size of 30x20 Km; same initial shear- and normal stress, nucleation and seismic array), the reference model was 40m87normal. As in previous Sections explained, we compare our PGV values (maximum horizontal component) and SA values (T=1s) with GMPE of BA08.

Model	Dip [°]	Mw	Mean PGV [cm/s]	Mean PSA [cm/s^2]
m86	30	6.904616	14.5207±10.6750	134.9748±85.34230
m87	40	6.897840	14.6276±10.2068	119.6868±83.36450
m88	60	6.900848	17.3300±13.4336	130.6941±99.96500
m89	80	6.929193	18.7691±18.2476	129.5129±134.3567
m91	70	6.914236	18.5335±16.1882	132.4408±118.5949
m92	50	6.895730	15.7035±10.9134	123.5404±083.8863
m93	35	6.901313	14.4835±10.4684	124.0040±085.3254
m94	45	6.895679	15.0172±10.2364	120.1507±081.6312
m95	88	6.945350	18.7888±19.0329	140.9336±138.5498

Table 4: Overview of dip-experiments: 30m86normal-80m89normal.

Numerical Errors caused by Mesh Deformation

In order to accommodate the case of dip-slip rupture on a dipping fault intersecting the free surface, we need to apply shearing in the plane defined by the fault surface normal and the slip vector. Shearing of this orientation does not effect the fault surface elements, and they remain rectangular. But volume elements are defected towards or away from the slip vector. Therefore it is important to understand the numerical affects of such a deformation. (Ely, Day et al. 2009) assessed numerical errors by comparing differently sheared mesh models to a reference rectangular mesh model. Their results indicate that the method remains highly accurate for applications with modest shearing up to 60° dipping normal faults (dip is defined as the angle between the horizontal and the fault plane). From the perspective of numerical errors resulting from the mesh shearing, we are doing a good job with a dip of 45° in our models.

Dip angle range in Nature

(Collettini and Sibson 2001) performed a dip estimation (n=23) that has been prepared from focal mechanisms of shallow, intracontinental, normal-slip earthquakes (M>5.5) where the rupture plane is unambiguously discriminated. The dip distribution for these moderate-to-large normal fault ruptures is in the range of 65°>dip>30°.

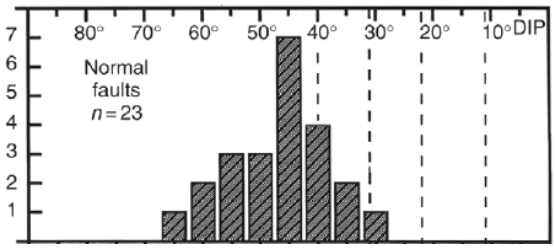

Figure 33: Dip estimation after (Collettini and Sibson 2001). The range of normal fault dip in nature is 30°-65°.

Normal Faulting in GMPE

GMPE for average horizontal-component ground motions of Boore & Atkinson (2008) is also a function of fault type (strike-slip, normal fault and reverse faulting). They were derived by empirical regression of an extensive strong-motion database compiled by the „PEER NGA“ (Pacific Earthquake Engineering Research Center's Next Generation Attenuation) at persiods between 0.01s and 10s. Data contained normal faults with dips between 30° and 80°, with a concentration between 40° and 60°. The data fitting should therefore exhibit smallest misfit in that range.

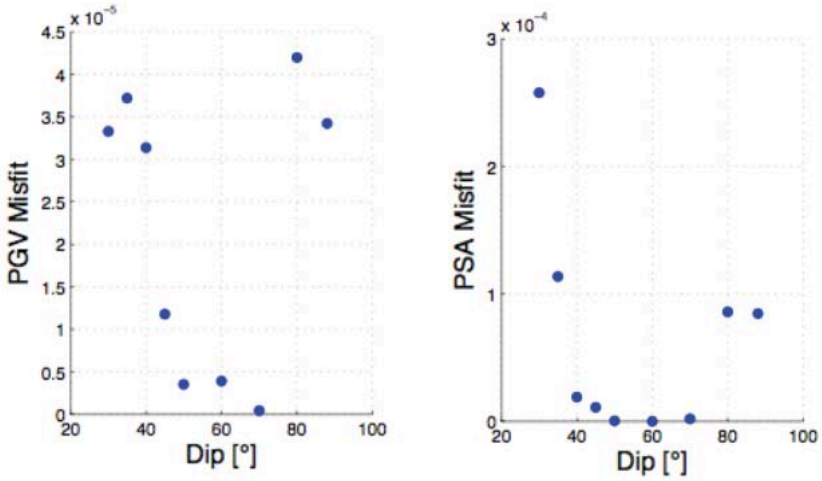

Figure 34: PGV and SA(T=1s) misfit showing minimum misfit at dips which served as a base of BA08 GMPE derivation.

Figure 34 shows PGV and PSA misfit (Formula 10) as a function of dip. Two groups are visible: a group with a large misfit (>1.5e-5) and a group with small misfit (<1.5e-5). Normal fault models with dips between 40° and 70° exhibit small misfits. The choice of 45° in our models seems therefore to be quite reasonable.

But what ist he impact of dip on moment magnitude, mean PGV and mean PSA? Results of our investigation are shonw in the following Figures.

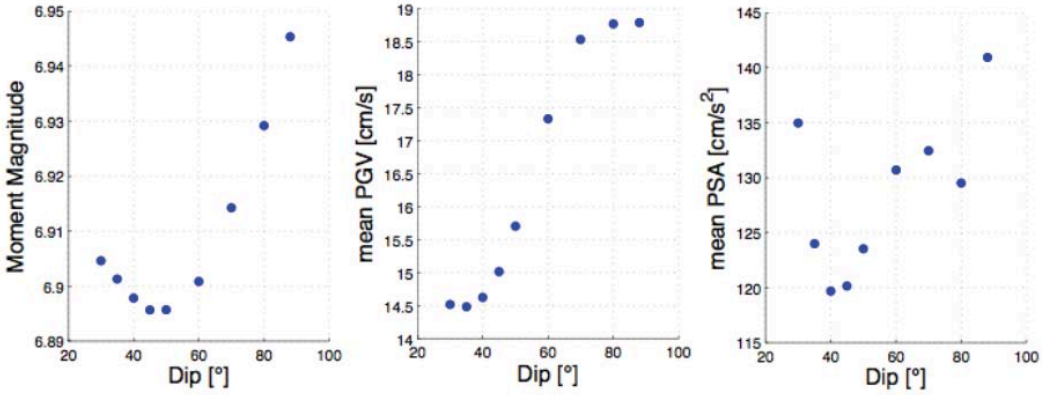

Figure 35: *Left:* Moment magnitude as a function of dip. *Centre:* Mean PGV as a function of dip. *Right:* Mean PSA as a function of dip.

Generally, the moment magnitude does not change significantly with varying dip. A change in dip has almost no impact on moment magnitude. Mean peak ground velocity increases with increasing dip. The difference between the maximum and minimum average mean PGV is 4.5cm/s, which is smaller than the PGV misfit variability of each model. An interesting feature is that the curve is flattens for smaller (<40°) and larger (>80°) dips. The evolution of mean PSA with increasing dip is more complicated. Beginning at small dips, mean PSA values decrease at the beginning before they start to increase again at 40° with increasing dip angle. The difference between maximum and minimum mean PSA is about 20m/s^2, which is much smaller than the variability of each model. In general, dip variation, particulary of about 45°±10°, does not affect moment magnitude or mean PGV/PSA significantly.

3.5 WHAT DO WE KNOW SO FAR?

Seismic Survey

Our data, gathered in several seismic surveys, expound the presence of a seismic anomaly. This anomaly is characterized by an amplitude reduction of seismic waves that penetrate the potential gauge zone and could be an indicator for a low-velocity-zone and therefore for a fault. We could detect this anomaly in three different surveys in the close proximity of Unterstalden. Furthermore geological data (observations at the surface and in the tunnel Eyholz) support results of seismic surveys. But there is so far no clear evidence for a fault or fault system south or southeast of Visp. Nevertheless, on the base of the survey data, we cannot exclude the existence for such a fault.

What determines the Magnitude of the Models?

We found that moment magnitude in our models is mainly determined by the size of the rupture area as well as the difference between static and dynamic coefficient of friction. Low Hurst exponent (<0.5) and small correaltion lengths (acx=acy<8Km) can enhance the effect of a small difference between static and dynamic coefficient of friction and lead to small moment magnitudes.

Our models are divided into two groups: low magnitudes (5.51≤Mw≤6.02) and large magnitudes (6.24≤Mw≤7.02). Looking at the rupture propagation, earthquake models from group 1 almost only generate nucleation part and do not generate sufficent propagating waves and therefore too low peak ground motion values (PGV, SA)

Comparison with GMPE

Considering different definitions for peak ground motion values (PGV & SA) and distances, data fit GMPE of Boore & Atkinson (BA08) much better than GMPE of Akkar & Bommar (AK10). Best fitting with BA08 was obtained by using maximum horizontal component and Joyner-Boore distances.

Best fitting of SA model data with BA08 was achieved at a period of T=1s, when misfit was minimal. For periods < 0.75s, misfit increases unreasonably such that only periods larger than 0.75s can be considered.

Generally, misfit decreases exponentially with increasing distance. Within the nearfield (<15Km), misfit is unreasonably large.

V OUTLOOK

As a final result, we intend to have a large number of different earthquake scenarios of normal and thrust faulting and strike-slip faults as well as buried and surface ruptured faults. The goal is to evaluate the variability of the earthquake scenarios in order to answer key questions (Section I). Furthermore, we want to know what are the magnitude-controlling parameters and their dependance. Last but not least, we want to find the signature of supershear in ground motions in order to assess seismic hazard.

VI APPENDIX

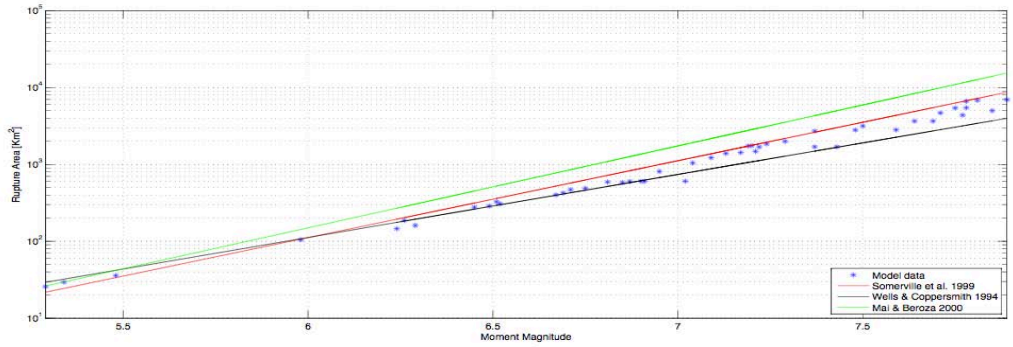

A1(a)

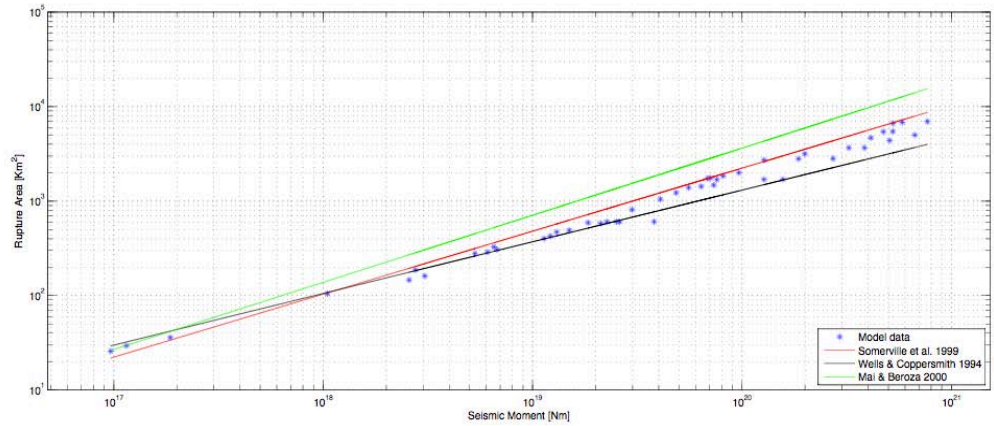

A1(b)

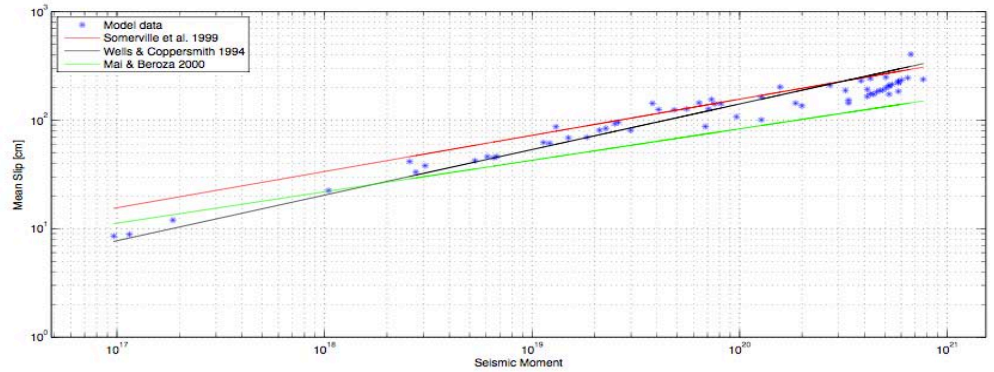

A1(c)

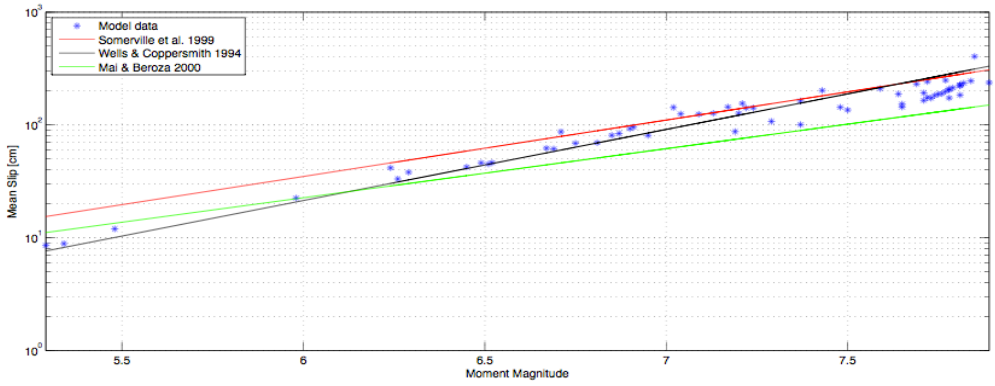

A1(d)

Mw=6.24-7.02: GMPE Analysis, PGV, DistRup

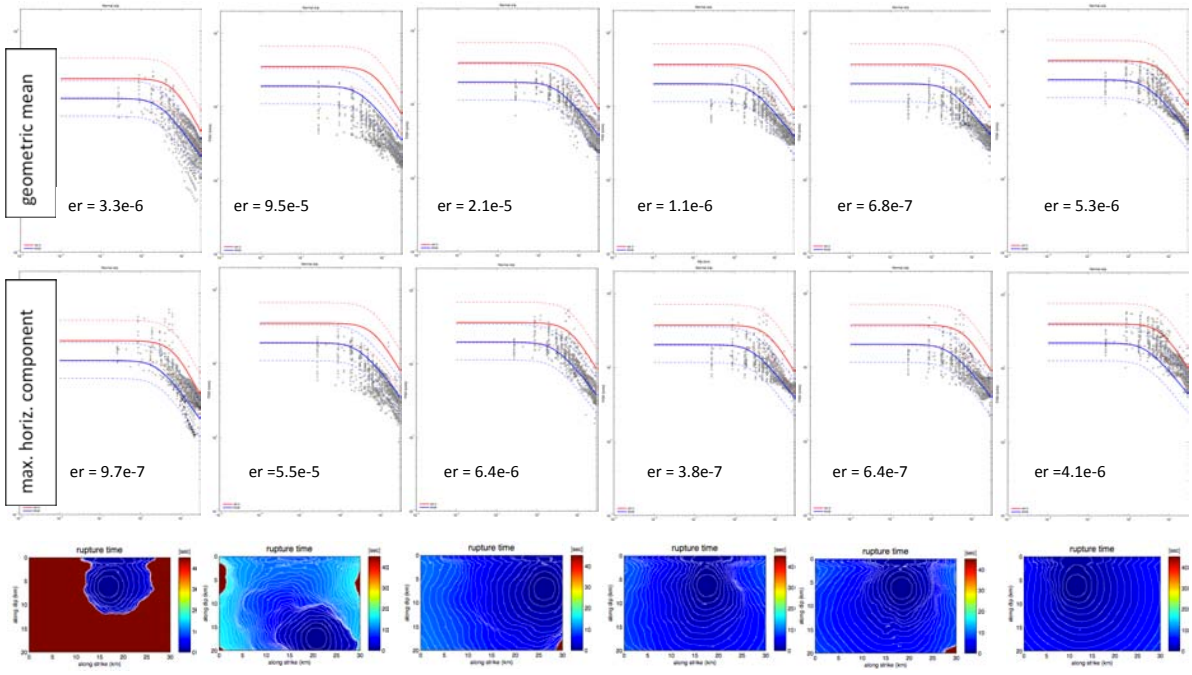

Mw=6.24 (m69) **Mw=6.81 (m73)** **Mw=6.87 (m71)** **Mw=6.9 (m74)** **Mw=6.91 (m70)** **Mw=7.02 (m72)**

A2(a)

Mw=5.51-6.02: GMPE Analysis, PGV, DistRup

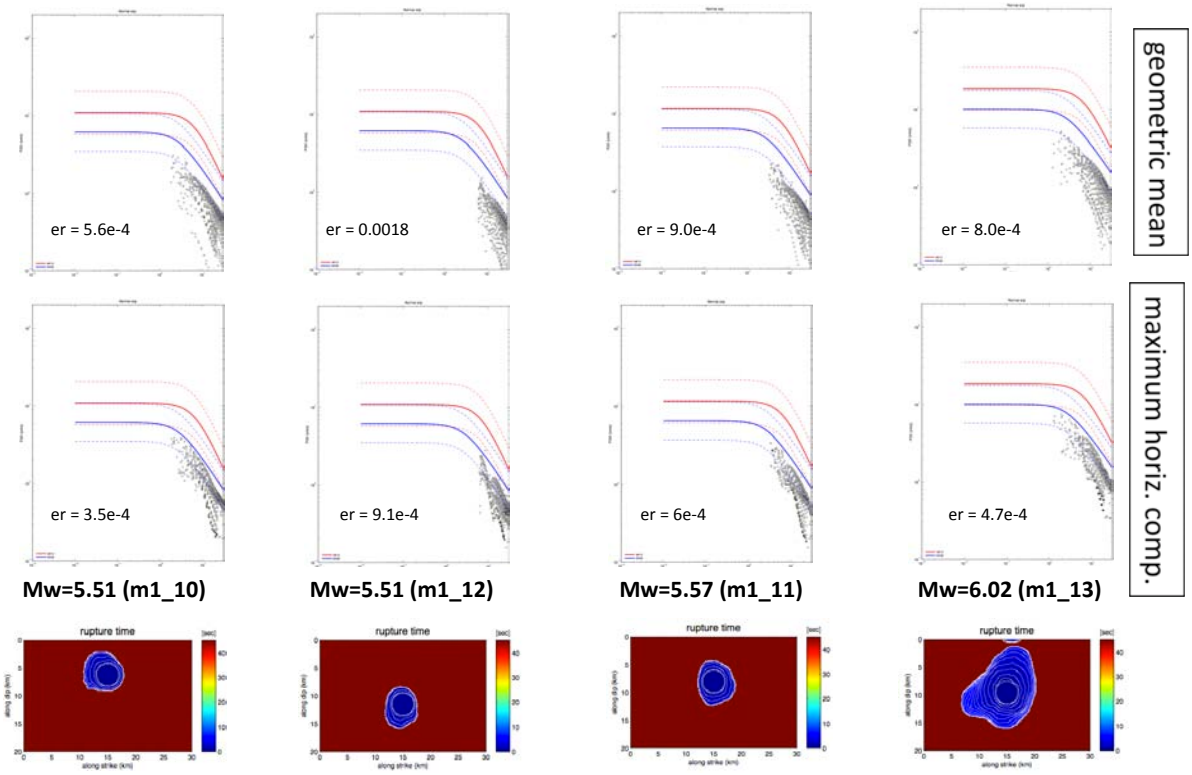

Mw=5.51 (m1_10) **Mw=5.51 (m1_12)** **Mw=5.57 (m1_11)** **Mw=6.02 (m1_13)**

A2(b)

Mw=6.24-7.02: GMPE Analysis, SA(T=1s), DistRup

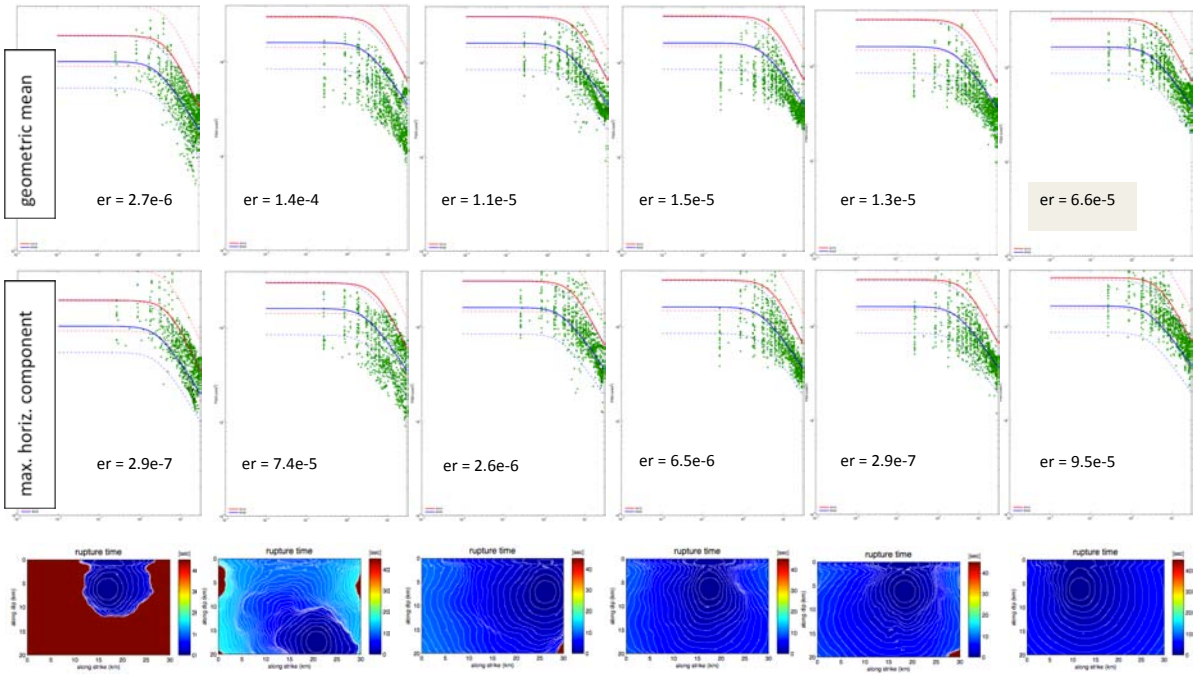

Mw=6.24 (m69) **Mw=6.81 (m73)** **Mw=6.87 (m71)** **Mw=6.9 (m74)** **Mw=6.91 (m70)** **Mw=7.02 (m72)**

A3(a)

Mw=5.51-6.02: GMPE Analysis, SA(T=1s), DistRup

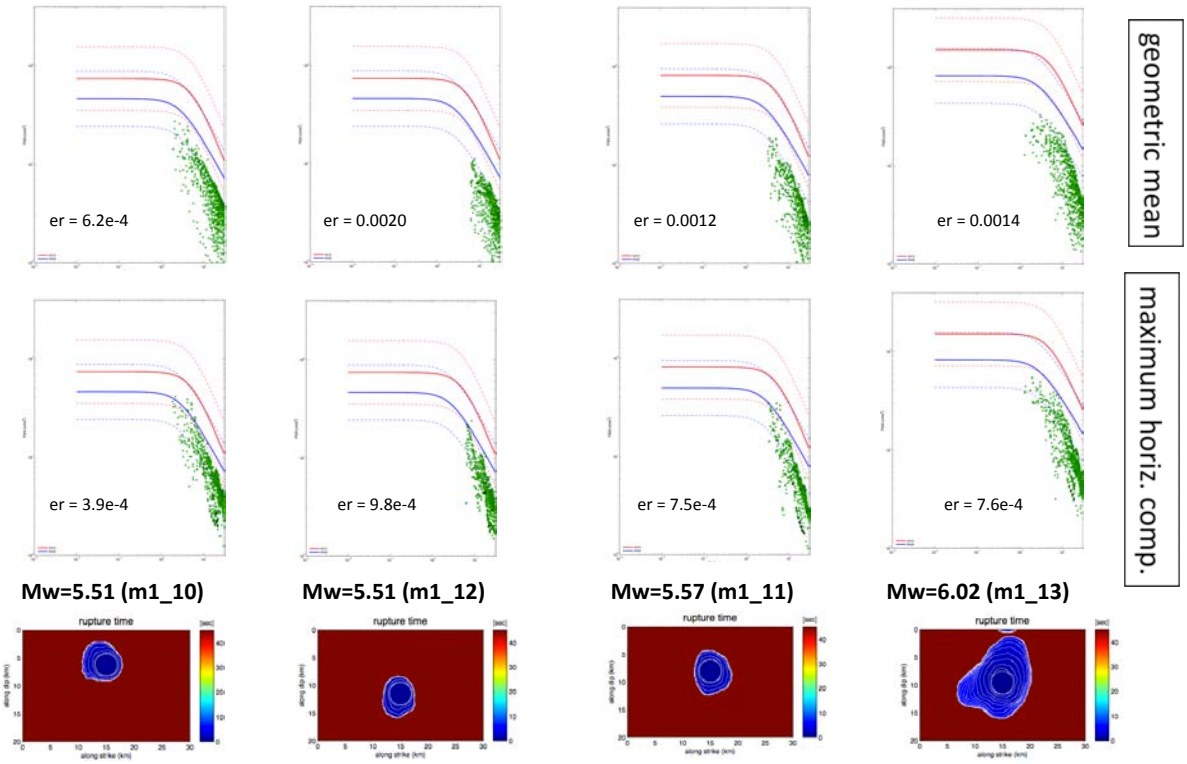

Mw=5.51 (m1_10) **Mw=5.51 (m1_12)** **Mw=5.57 (m1_11)** **Mw=6.02 (m1_13)**

A3(b)

Mw=5.51-7.02: Misfit vs. Distance, PGV, JB, max. horiz. comp.

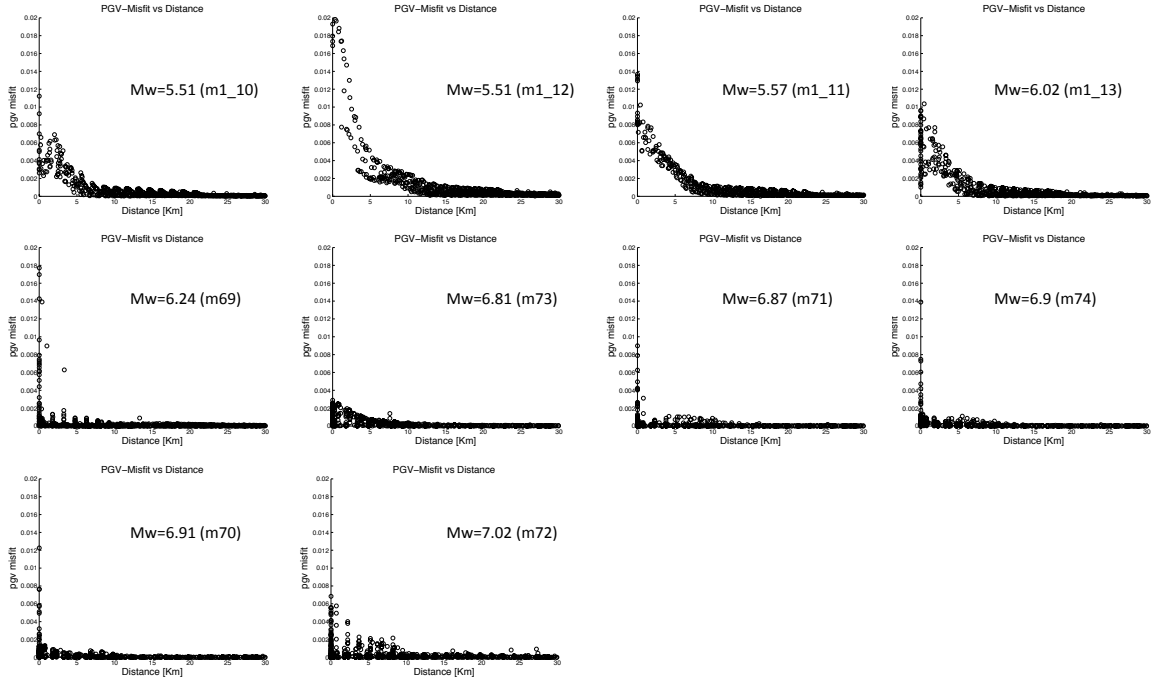

A4(a)

Mw=5.51-7.02: Misfit vs. Distance, SA(T=1s), JB, max. horiz. comp.

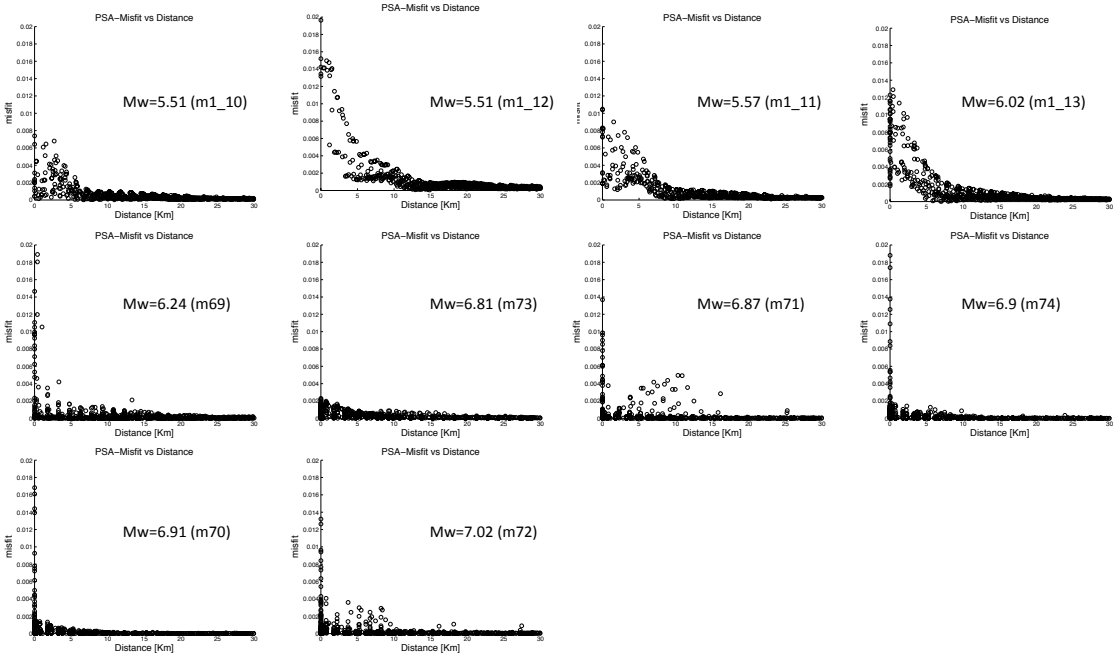

A4(b)

Mw=5.51-7.02: Misfit vs. Distance, PGV, JB, geometric mean.

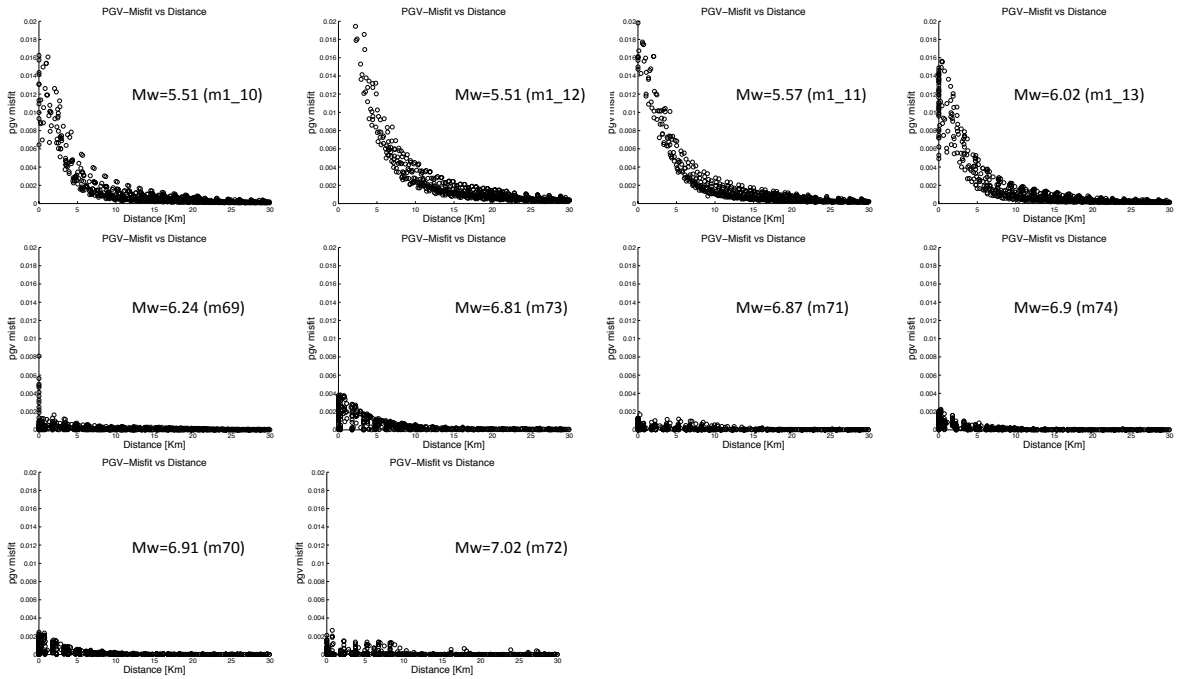

A5(a)

Mw=5.51-7.02: Misfit vs. Distance, SA(T=1s), JB, geometric mean

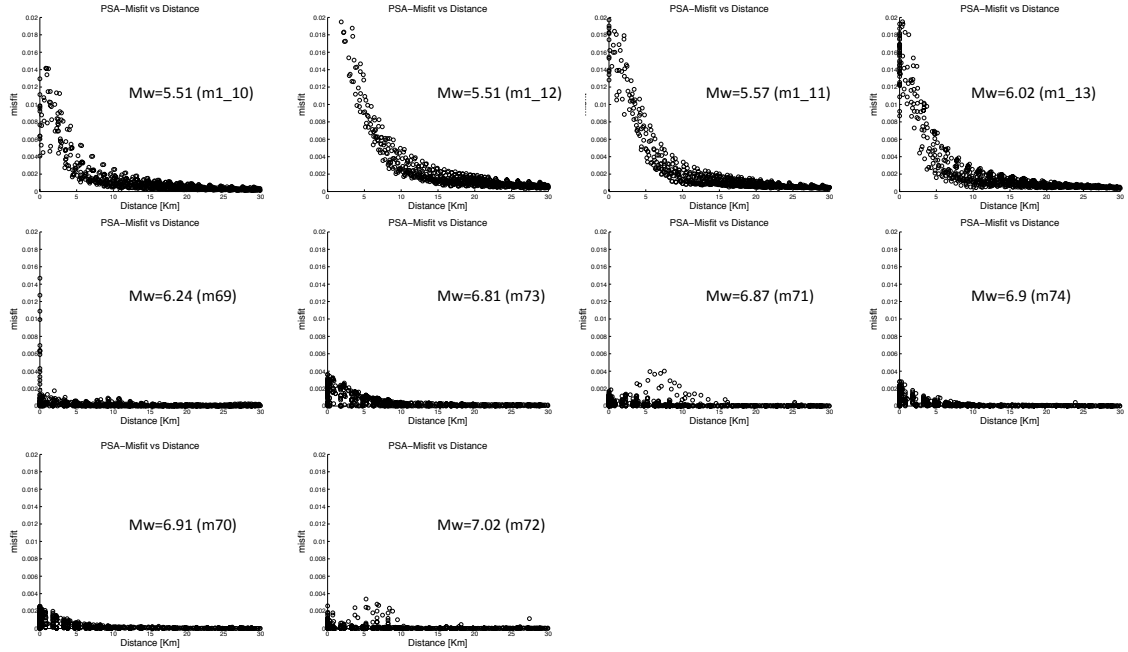

A5(b)

A6

GENERAL FAULT PARAMETERS	
Buried fault depth [Km]	0
Sampling in x- and z-direction [Km]	0.1 0.1
Cohesion force [MPa]	1.0
LOADING PARAMETERIZATION	
Depth of max. loading/unloading [Km]	15
Max. loading/unloading on principal stress Sigma1 [MPa]	50
Angle with max. principal stress for strike vertical slip [MPa]	45
Normal stress value (if value above is zero) [MPa]	120
SHALLOW DEPTH CHARACTERIZATION	
Depth width of strength hardening region [Km]	2.0
Negative stress drop on the free-surface [MPa]	-2.0
Min. strength excess in strength. area [MPa]	1.0
Max. critical slip distance on the free surface [m]	5
Water density [Kg/m3]	1000
Depth, where critical slip distance starts to increase [Km]	20
Max. critical slip distance at depth where dc starts to incr. [m]	10
Percentage of breakdown strengthdrop for overloading nucleation or drop static strength	2
1 = static strengt his drop below initial stress 0 = initial stress is overloaded	0

VII REFERENCES

Akkar, S. and J. J. Bommer (2010). "Empirical equations for the prediction of PGA, PGV, and spectral accelerations in Europe, the Mediterranean region, and the Middle East." Seismological Research Letters **81**(2): 195.

Boore, D. M. and G. M. Atkinson (2008). "Ground-motion prediction equations for the average horizontal component of PGA, PGV, and 5%-damped PSA at spectral periods between 0.01 s and 10.0 s." Earthquake Spectra **24**: 99.

Borcherdt, R. D. (1994). "Estimates of site-dependent response spectra for design (methodology and justification)." Earthquake Spectra **10**(04).

Byerlee, J. (1978). "Friction of rocks." Pure and applied geophysics **116**(4): 615-626.

Cabrera, B. M. (2010). Physic-based classification, quantification, and simulation of ground motion for earthquake engineering applications, ETH.

Campani, M. (2009). Temporal and spatial evolution of a syn-orogenic extensional system: the Simplon Fault Zone (Central Alps), ETH.

Chester, F. and J. Logan (1986). "Implications for mechanical properties of brittle faults from observations of the Punchbowl fault zone, California." Pure and applied geophysics **124**(1): 79-106.

Collettini, C. and R. H. Sibson (2001). "Normal faults, normal friction?" Geology **29**(10): 927.

Dalguer, L. A. and S. M. Day (2007). "Staggered-grid split-node method for spontaneous rupture simulation." J. geophys. Res **112**: B02302.

Day, S. M. (1982). "Three-dimensional finite difference simulation of fault dynamics: rectangular faults with fixed rupture velocity." Bulletin of the Seismological Society of America **72**(3): 705-727.

Deichmann, N. (2003). "Focal depths of earthquakes below Switzerland." Swiss Seismol: 1-4.

Ely, G. P., S. M. Day, et al. (2008). "A support-operator method for viscoelastic wave modelling in 3-D heterogeneous media." Geophysical Journal International **172**(1): 331-344.

Ely, G. P., S. M. Day, et al. (2009). "A support-operator method for 3-D rupture dynamics." Geophysical Journal International **177**(3): 1140-1150.

Fritsche, S. (2008). "Large historical earthquakes in Switzerland." Multidisciplinary Studies on Damage Fields and Site Effects, Diss. ETH Zürich(17710).

Harris, R., M. Barall, et al. (2009). "The SCEC/USGS dynamic earthquake rupture code verification exercise." Seismological Research Letters **80**(1): 119.

Kastrup, U., M. L. Zoback, et al. (2004). "Stress field variations in the Swiss Alps and the northern Alpine foreland derived from inversion of fault plane solutions."

Kozák, J. and J. Vaněk (2006). "The 1855 VISP (Switzerland) earthquake: Early attempts of earthquake intensity classification." Studia geophysica et geodaetica **50**(1): 147-160.

Mai, P. M. and G. C. Beroza (2000). "Source scaling properties from finite-fault-rupture models." Bulletin of the Seismological Society of America **90**(3): 604.

Mai, P. M. and G. C. Beroza (2002). "A spatial random field model to characterize complexity in earthquake slip." J. geophys. Res **107**(10.1029): 2001.

Marchant, R. (1993). The underground of the Western Alps, Université de Lausanne.

Marone, C. (1998). "Laboratory-derived friction laws and their application to seismic faulting." Annual Review of Earth and Planetary Sciences **26**(1): 643-696.

Prieto, G., R. Parker, et al. (2009). "A Fortran 90 library for multitaper spectrum analysis." Computers & Geosciences **35**(8): 1701-1710.

Ripperger, J., P. Mai, et al. (2008). "Variability of near-field ground motion from dynamic earthquake rupture simulations." Bulletin of the Seismological Society of America **98**(3): 1207-1228.

Samarskii, A. (1982). "Operational Finite-Difference Schemes." DIFFERENTIAL EQUAT. **17**(7): 854-862.

Shashkov, M. (1996). "Conservative Finite-Difference Methods on general grids." CRC Press, Boca Raton, FL.

Somerville, P., K. Irikura, et al. (1999). "Characterizing crustal earthquake slip models for the prediction of strong ground motion." Seismological Research Letters **70**(1): 59.

Virieux, J. (1986). "P-SV wave propagation in heterogeneous media: velocity-stress finite-difference method." Geophysics **51**(4): 889-901.

Waldhauser, F. (1996). A parametrized three-dimensional Alpine crustal model and its application to teleseismic wavefront scattering, Ph. D. Thesis.

Waldhauser, F., E. Kissling, et al. (1998). "Three-dimensional interface modelling with two-dimensional seismic data: the Alpine crust–mantle boundary." Geophysical Journal International **135**(1): 264-278.

Wells, D. L. and K. J. Coppersmith (1994). "New empirical relationships among magnitude, rupture length, rupture width, rupture area, and surface displacement." Bulletin of the Seismological Society of America **84**(4): 974-1002.

Werenfels, A. (1924). "Geologische Beschreibung der Lepontinischen Alpen." Beiträge zur geologischen Karte der Schweiz **3. Teil**.

Synthetic broadband ground motion database of two normal faulting models for Visp Area

Authors of simulations: Luis A. Dalguer (SED-ETH) and Martin Mai (KAUST-Saudi Arabia)

Contact: Luis A. Dalguer, e-mail: dalguer@sed.ethz.ch

Date: November 21, 2011

Models: Data of fully physics-based near-field synthetic seismograms in a wide frequency band (up to~50 Hz), that combines spontaneous dynamic rupture modeling (Dalguer and Mai, 2011) with a high-frequency seismic-scattering approach seismograms (Mai and Dalguer, 2011) on a dense near-source receiver grid .
From a suit of 360 models, we have selected two normal faulting models with dip=60°

1) s1normal, buried rupture with depth dependent normal stress (Mw=6.53)
2) s16normal, surface rupture with depth dependent normal stress (Mw=6.55)

Reference: Explanation on model parameterization and fault geometry can be found in the following references (pdf file of them is in the directory references):
-Dalguer L.A. and P. M. Mai (2011), Near- Source Ground Motion Variability from M~6.5 Dynamic Rupture Simulations. *4th IASPEI / IAEE International Symposium: Effects of Surface Geology on Seismic Motion,* In CD. August 23–26, 2011, University of California Santa Barbara, CA, USA.

- Mai P. M. and L.A. Dalguer (2011), Broadband Ground-Motion from Rupture Dynamic. *4th IASPEI / IAEE International Symposium: Effects of Surface Geology on Seismic Motion*, In CD. August 23–26, 2011, University of California Santa Barbara, CA, USA.

DATA

-The data is located in two subdirectories:
/buried_depth/ for the buried rupture model (s1normal)
/surface_depth/ for the surface rupturing model (s16normal)

-Source parameters and 168 stations location data. They are in ASCII format, located respectively for s1normal and s16normal models in:
/buried_depth/stations_fault_distance/s1normal.stations.dat
/surface_depth/stations_fault_distance/s16normal.stations.dat

The ACII data is as follow:

% Source and stations data for PRP-Project (buried fault, depth dependent)
% Earthquake model = s1normal
% hypocenter (km) (x,y,z) = -10.000000 4.750000 13.227241
% Moment magnitude (Mw) = 6.53
% Seismic moment (1e19 New-m) = 0.77
% Average slip (m) = 0.62
% Maximum slip (m) = 1.37
% Average slip rate (m/s) = 0.75
% Maximum slip rate (m/s) = 2.28
% Ruprure area (km2) = 364.100000
% Average rupture speed (km/s) = 1.90
% Average stress drop (MPa) = 1.716544

% Max stress drop (MPa) = 10.617145
% Min stress drop (MPa) = -10.514810
% 1st column = station number
% 2nd column = Along strike distance in km
% 3rd column = Fault normal distance in km
% 4th column = Joyner-Boore Distanc (DistanceJB) in km
% 5th column = Shortest distance to the Rupture Surface (DistanceRup) in km
% 6th column = shortest horizontal distance to the line defined by extending the Fault Trace (DistanceX)
% 7th column = Side of the fault (0=footwall, 1=hanging wall)
% ==========

1	15.000000	0.300000	4.701064	8.708182	1.750000	1
2	14.800000	0.600000	4.382921	8.561916	2.050000	1
3	14.500000	0.800000	4.024922	8.362439	2.250000	1

…..
….
….

Figure 1 and 2 show respectively station distribution for the "s1normal" (buried) and "s16normal" (surface rupturing) rupture models

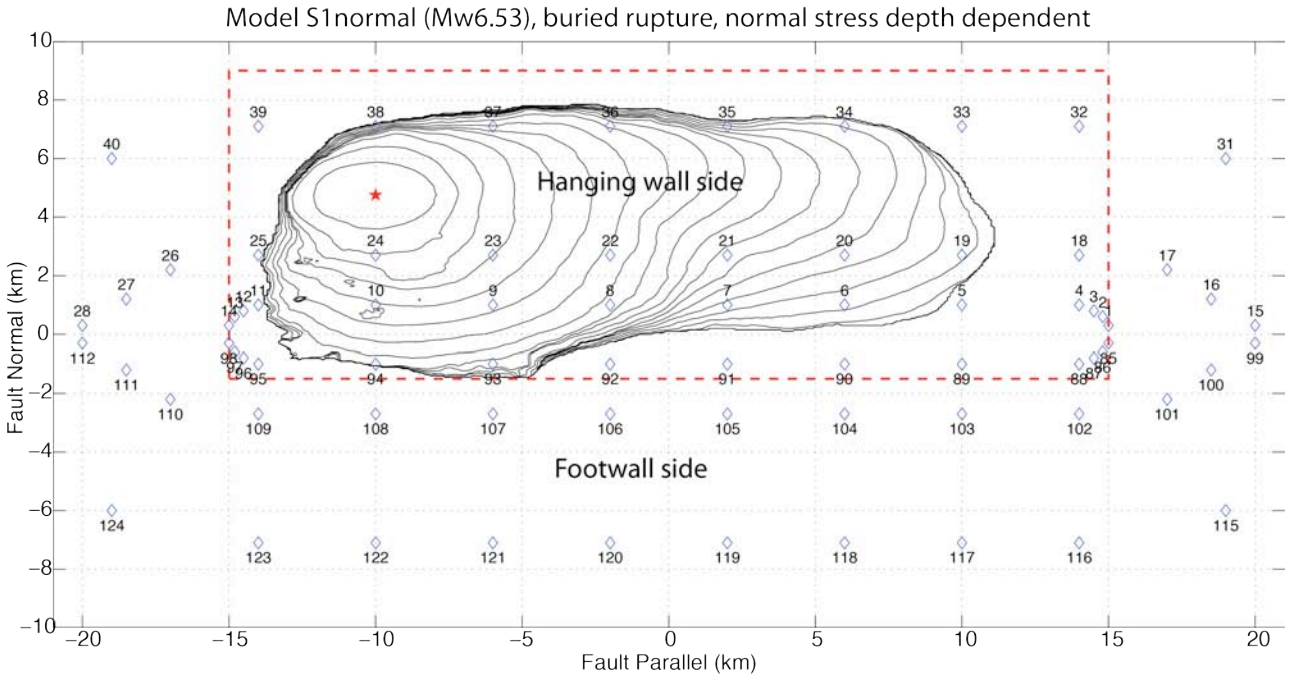

Figure 1a. Close up of station location around the fault and contour rupture time of the buried fault rupture of model ***s1normal.*** The dotted red line is the vertical projection of maximum allowed fault rupture plane. Red star denotes epicenter location.

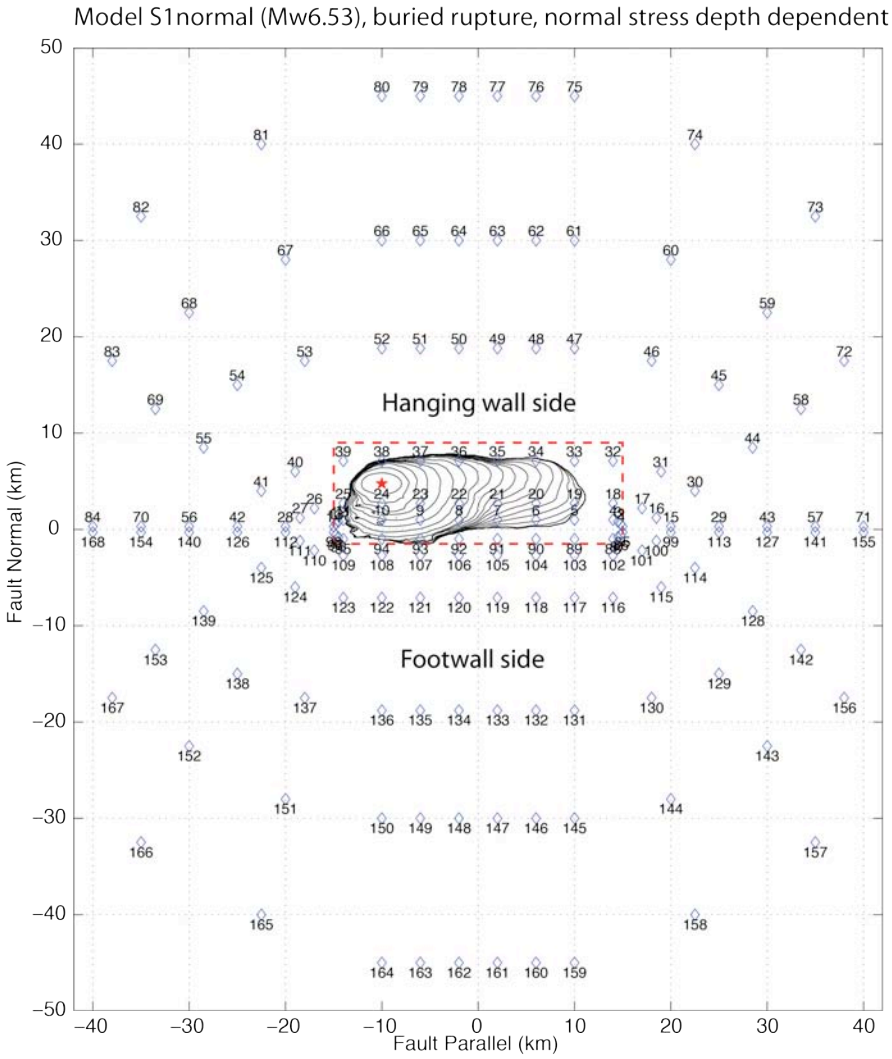

Figure 1b. The same as Figure 1a, but with far station location around the fault

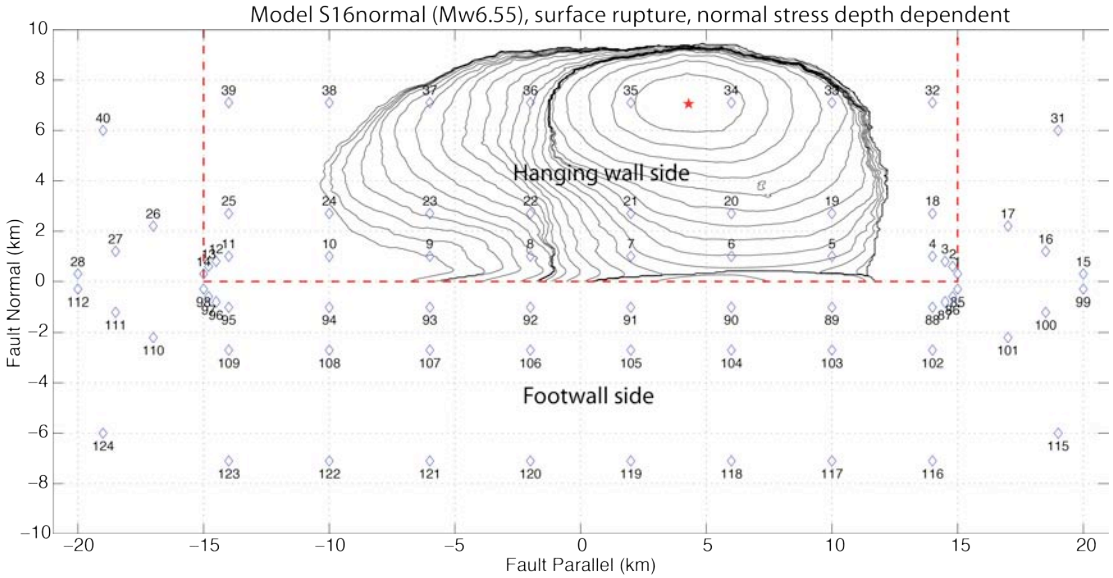

Figure 2a. Close up of station location around the fault and contour rupture time of the surface rupturing fault model ***s16normal.*** The dotted red line is the vertical projection of maximum allowed fault rupture plane. Red star denotes epicenter location.

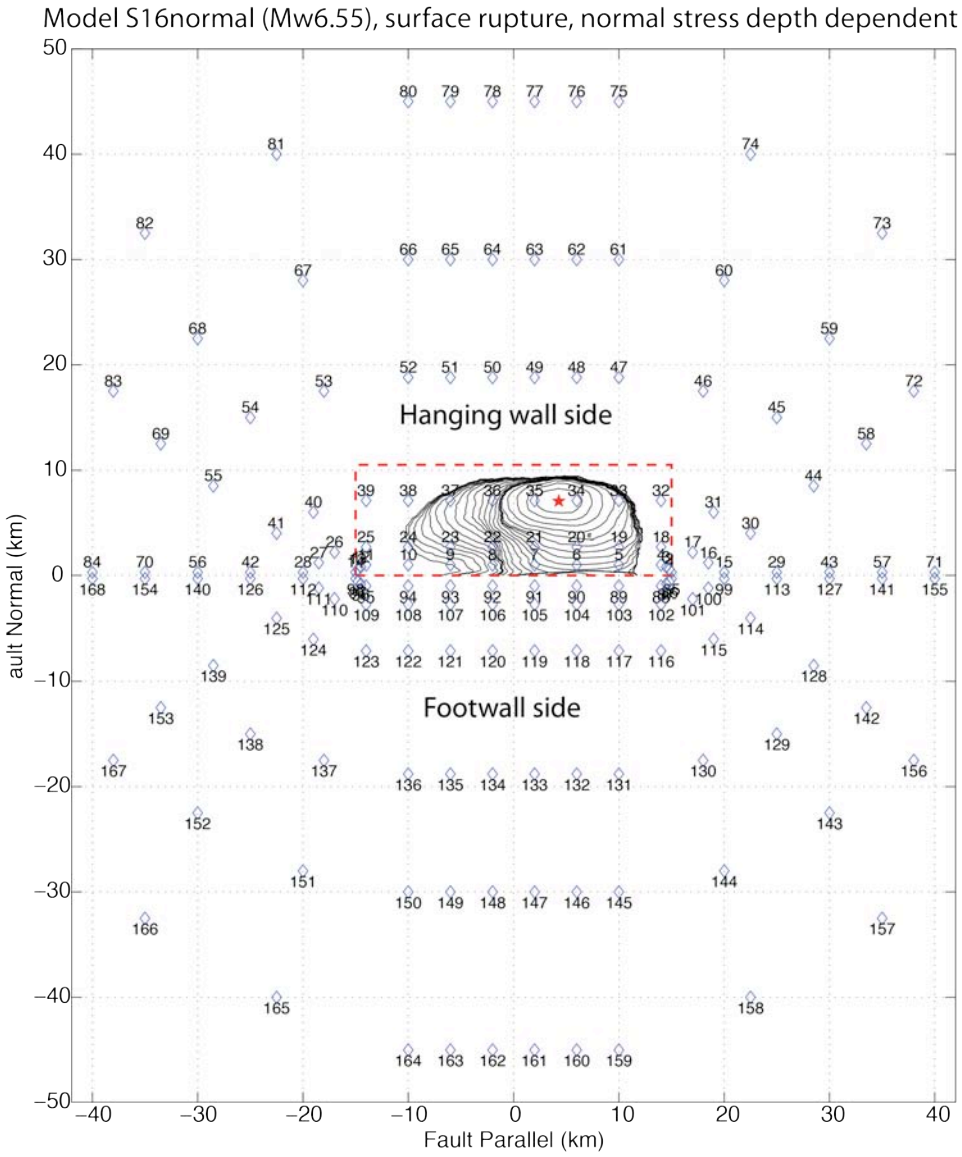

Figure 2b. The same as Figure 2a, but with far station location around the fault.

-Rupture models accommodated to the Visp area: The fault ruptures and stations distribution shown above (in figure 1 or 2) was accommodated in the Visp area at four locations:

1) *At fault rupture of 1855 earthquake (M~6.2?)*, shown in Figure 3, in which a seismic survey to identify the fault has been developed
2) *At fault rupture of 1755 earthquake (M~5.7?)*, shown in Figure 4
3) *At fault rupture of 1685 earthquake (M~5.3?)*, shown in Figure 5
4) *At simplon fault*, shown in Figure 6

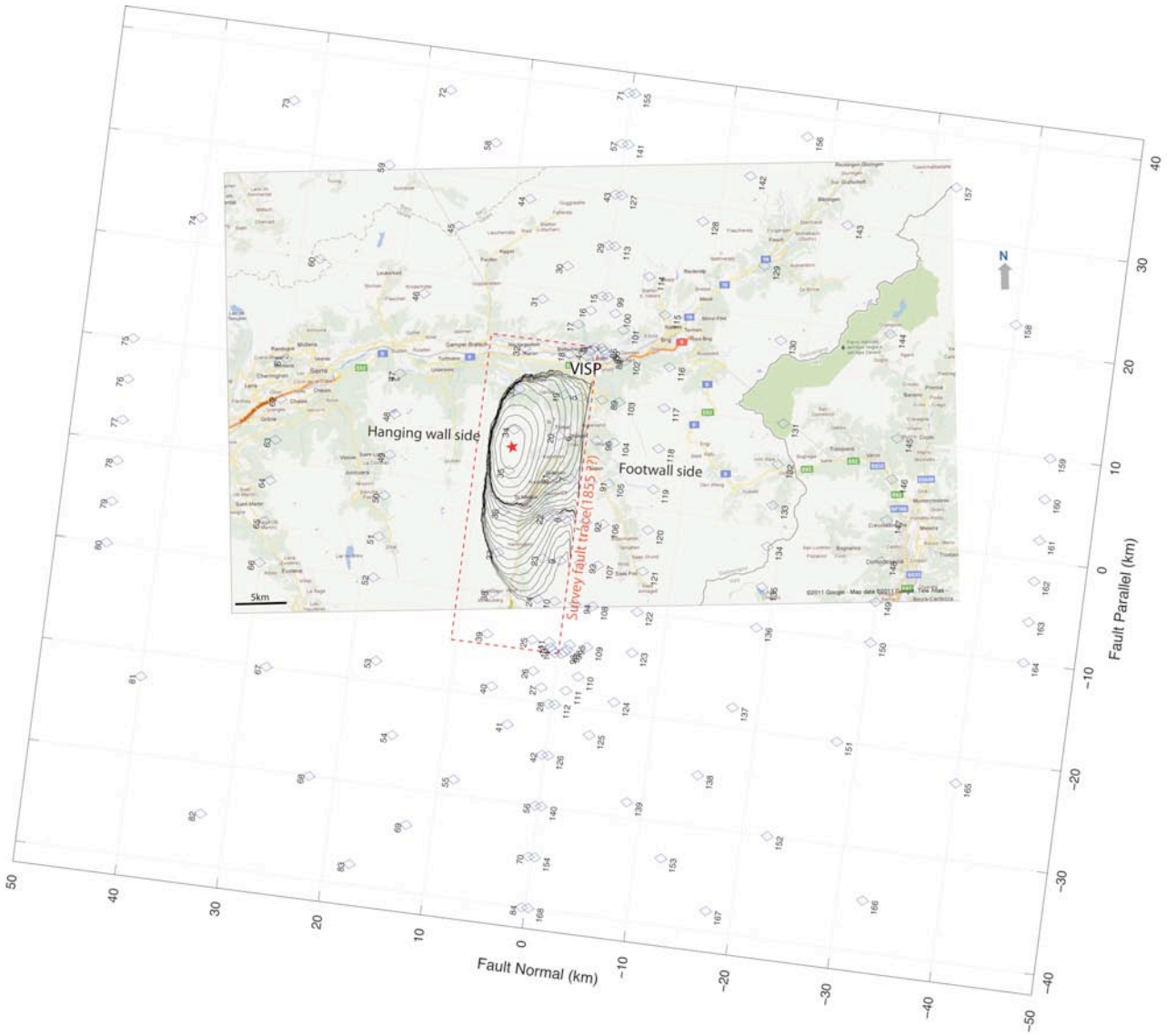

Figure 3. Fault rupture model and station distribution accommodated at the zone where the 1855 earthquake (M~6.2?) may has occurred. The dotted red line is the vertical projection of maximum allowed fault rupture plane in the model. The contour line represents the rupture time of the surface rupturing fault model ***s16normal*** (see figure 2). See Figure 1 or 2 for details of station distribution and fault ruptures.

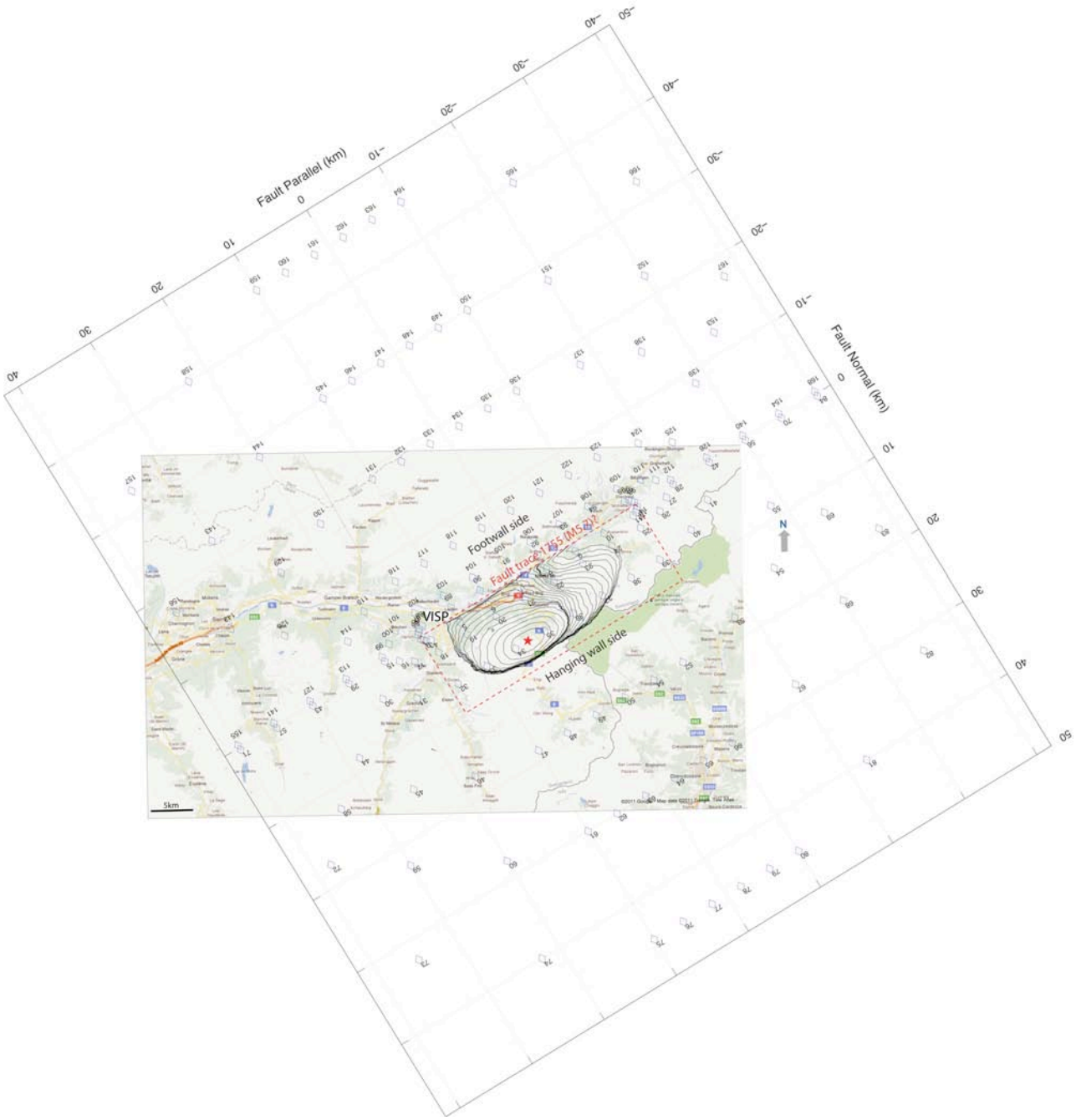

Figure 4. Fault rupture model and station distribution accommodated at the zone where the 1755 earthquake (M~5.7?) may has occurred. The dotted red line is the vertical projection of maximum allowed fault rupture plane in the model. The contour line represents the rupture time of the surface rupturing fault model ***s16normal*** (see figure 2). See Figure 1 or 2 for details of station distribution and fault ruptures.

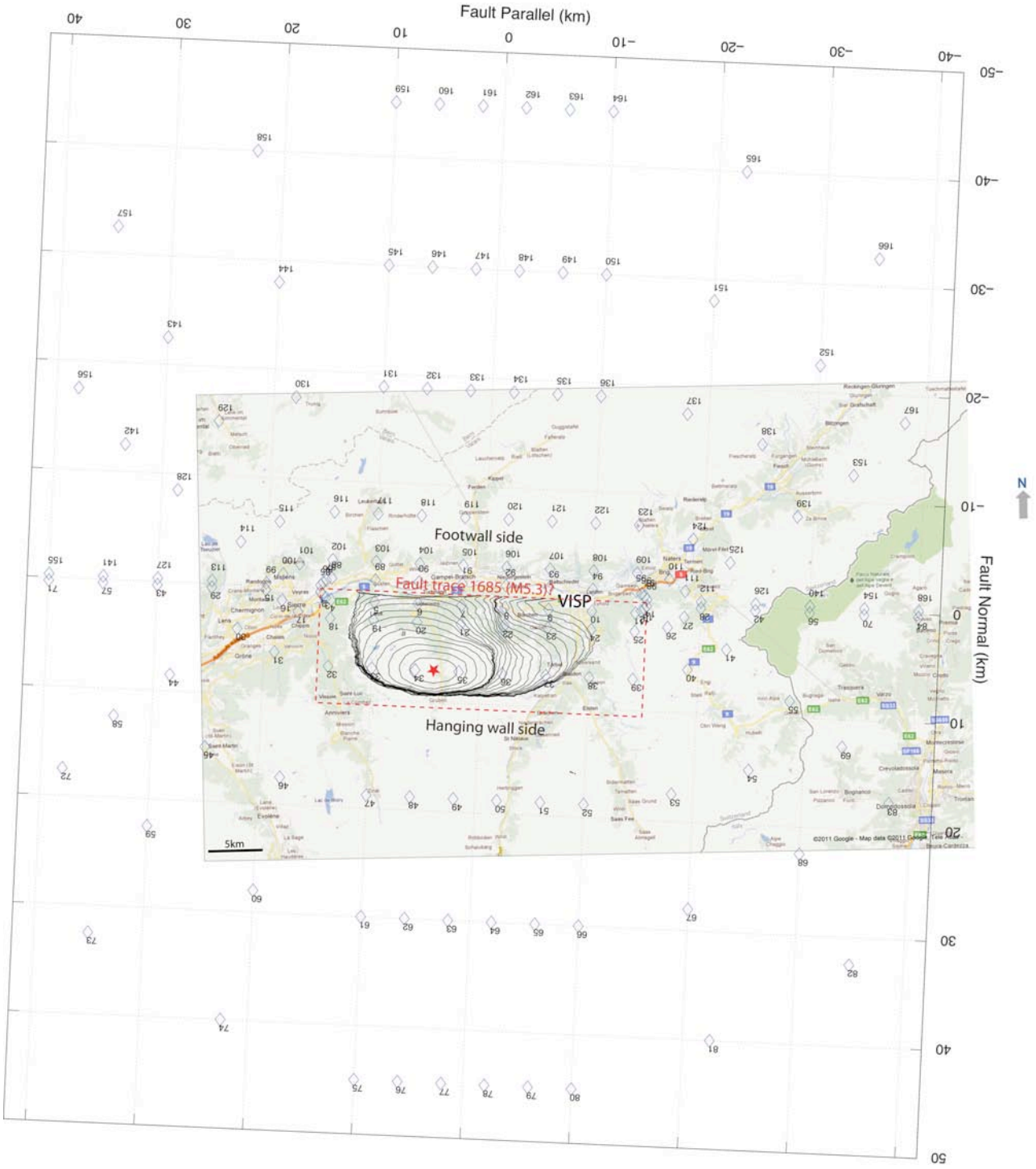

Figure 5. Fault rupture model and station distribution accommodated at the zone where the 1685 earthquake (M~5.3?) may has occurred. The dotted red line is the vertical projection of maximum allowed fault rupture plane in the model. The contour line represents the rupture time of the surface rupturing fault model ***s16normal*** (see figure 2). See Figure 1 or 2 for details of station distribution and fault ruptures.

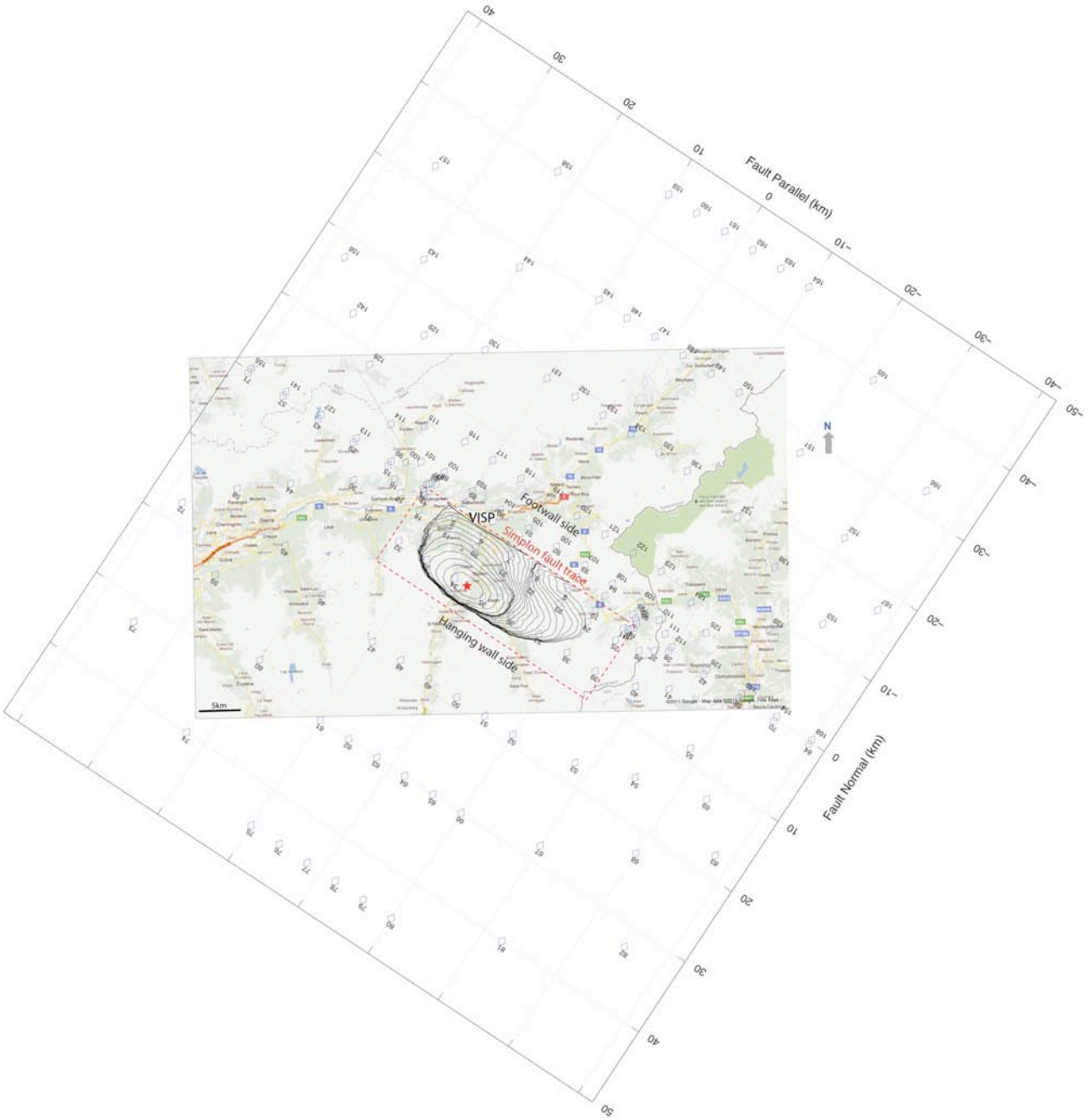

Figure 6. Fault rupture model and station distribution accommodated at the zone of the Simplon fault trace. The dotted red line is the vertical projection of maximum allowed fault rupture plane in the model. The contour line represents the rupture time of the surface rupturing fault model ***s16normal*** (see figure 2). See Figure 1 or 2 for details of station distribution and fault ruptures.

-Broadband of velocity ground motion data. The synthetic ground motions were generated for a reference Swave velocity of 2500m/s. The data in ASCII format is located respectively for s1normal and s16normal models in:
/buried_depth/s1normal/BBk1Qt**/hybrid/BB.s1n_****.hyb
/ surface_depth /s16normal/BBk1Qt**/hybrid/BB.s16n_****.hyb

where:
** is "fw" or "hw" for footwall and hanging wall respectively

**** is "fw/hw + station number with two digits (i.e. fw02)

Each file has a brief header that allows to immediately understand the format of it. An example of it for file "BB.s1n_hw84.hyb" is:

```
% ------------------------------------------------
% synthetic broadband seismogram (Mai&Olsen 2008)
% N = 8 header lines
% site:    s1n_hw84
% NPTS, DT:  16384 0.002929378068  (NPTS=number of samples, DT=time step)
%
 % time(s)      NS (m/s)      EW(m/s)     UP (m/s)
 % ------------------------------------------------
  0.00000    0.00000E+00    0.00000E+00    0.00000E+00
  0.00293    0.00000E+00    0.00000E+00    0.00000E+00
…
…
…
```

-Notice that NS = fault parallel component, EW=fault normal component, UP vertical component (downward positive).
-The number of stations for the hanging wall and footwall is 84, with a total of 168 stations (see figures 1 and 2 for location of them around the fault). This number of stations for each side of the fault is absolutely true for a surface-rupturing model. However, for a buried rupture model it depends of how rupture has extended on the allowed fault plane rupture.

MATLAB SCRIPTS to read data. Matlab scripts have to be run from the main directory /BBGmotionModels/

-**readBBvelf.m:** Function to read three component of Broad Band Velocity wave forms of of s1model for buried rupture and s16model for surface rupture.

-**BBAccVelDisp.m:** Function to calculate 3 component of acceleration, velocity and displacement of s1model for buried rupture and s16model for surface rupture

-BBPgvPgaSaGMPE.m: Function to calculate PGV, PGA and PSA at period T for all stations (168) and compare with GMPEs from Akkar and Bommer (2010) denoted as AK10 and Boore and Atkinson (2008) denoted as BA08. The synthetic ground motion data is for a reference S wave velocity for the current data is 2500m/s. For vs30 <= 1500 m/s it is estimated a Site-amplification corrections using the period dependent amplification coefficient of Borcherdt (1994, 2002). Figure 7 and 8 shows an example of the PGA and PGV compared with the GMPES for Vs30=1500m/s.

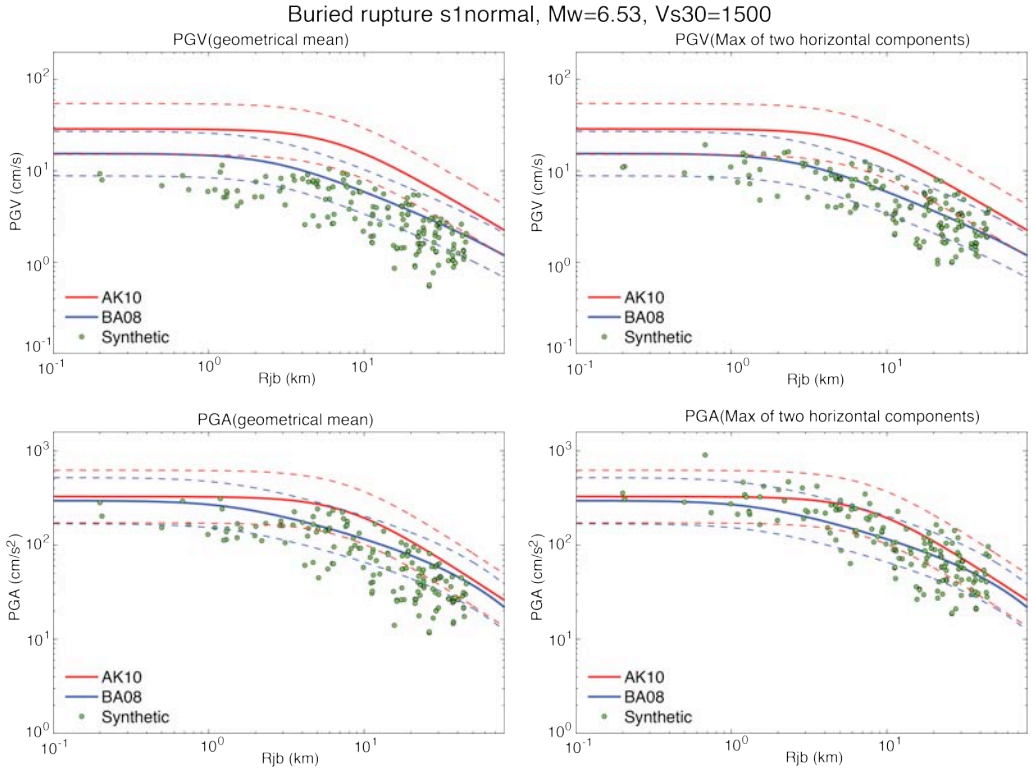

Figure 7. Horizontal PGV (top) and PGA (bottom) of buried rupture model "s1normal" compared with GMPE from AK10 (Akkar and Bommer, 2010) and BA08 (Boore and Atkinson, 2008) for Vs30=1500m/s. Peak values of synthetic wave forms are calculated in two ways: geometrical means (left figures) and maximum of two horizontal components (right figures)

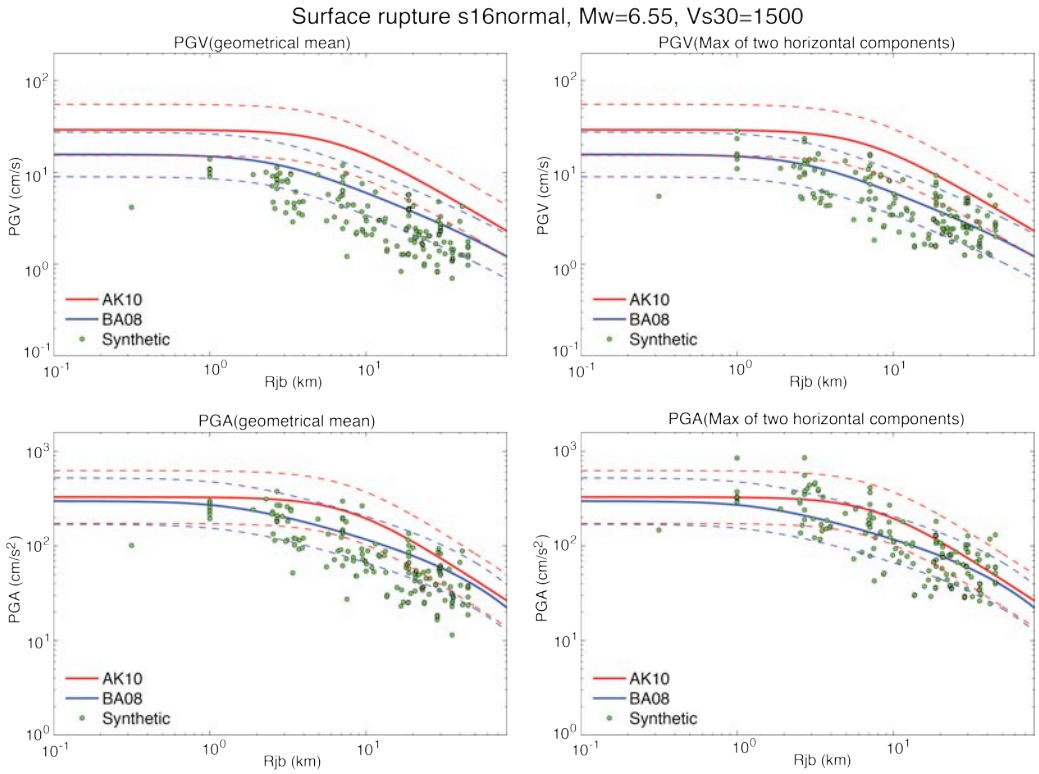

Figure 8. Horizontal PGV (top) and PGA (bottom) of Surface rupture model "s16normal". Specifications are the same as in Figure 7.

Other matlab scripts are included in the set of files to support calculations of the three matlab scripts described above.

Dynamic rupture solutions of "s1normal" and "s16normal" models

Figure 9 and 10 show respectively for s1normal and s16 normal the dynamic rupture solutions of slip, peak slip rate, rupture time and stress drop distribution.

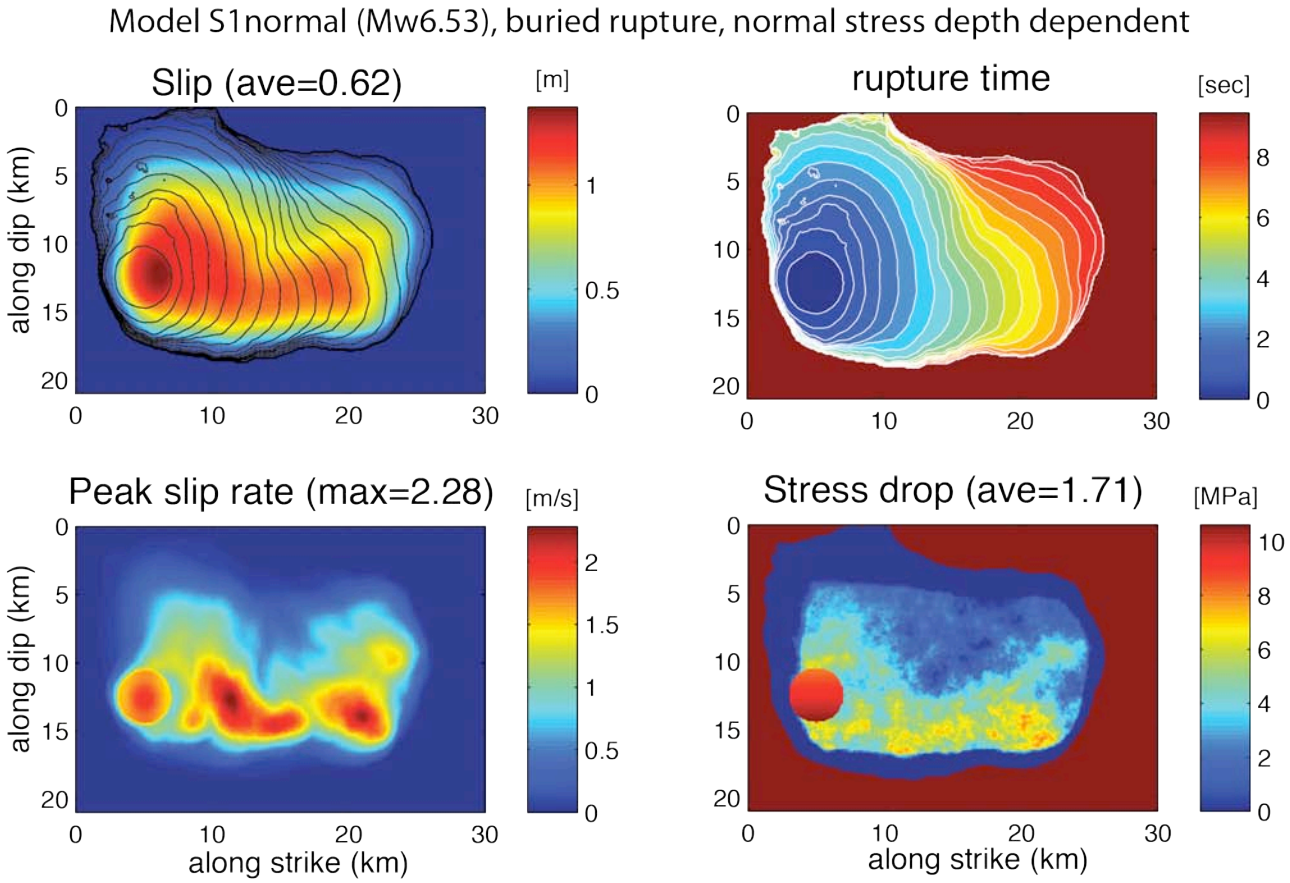

Figure 9. Dynamic rupture solutions for the buried rupture model "s1normal". Top left shows slip distribution (contour line is the rupture time each 0.5 sec); top right is image map and contour line of rupture time; bottom left is peak slip rate; and bottom right is the stress drop distribution.

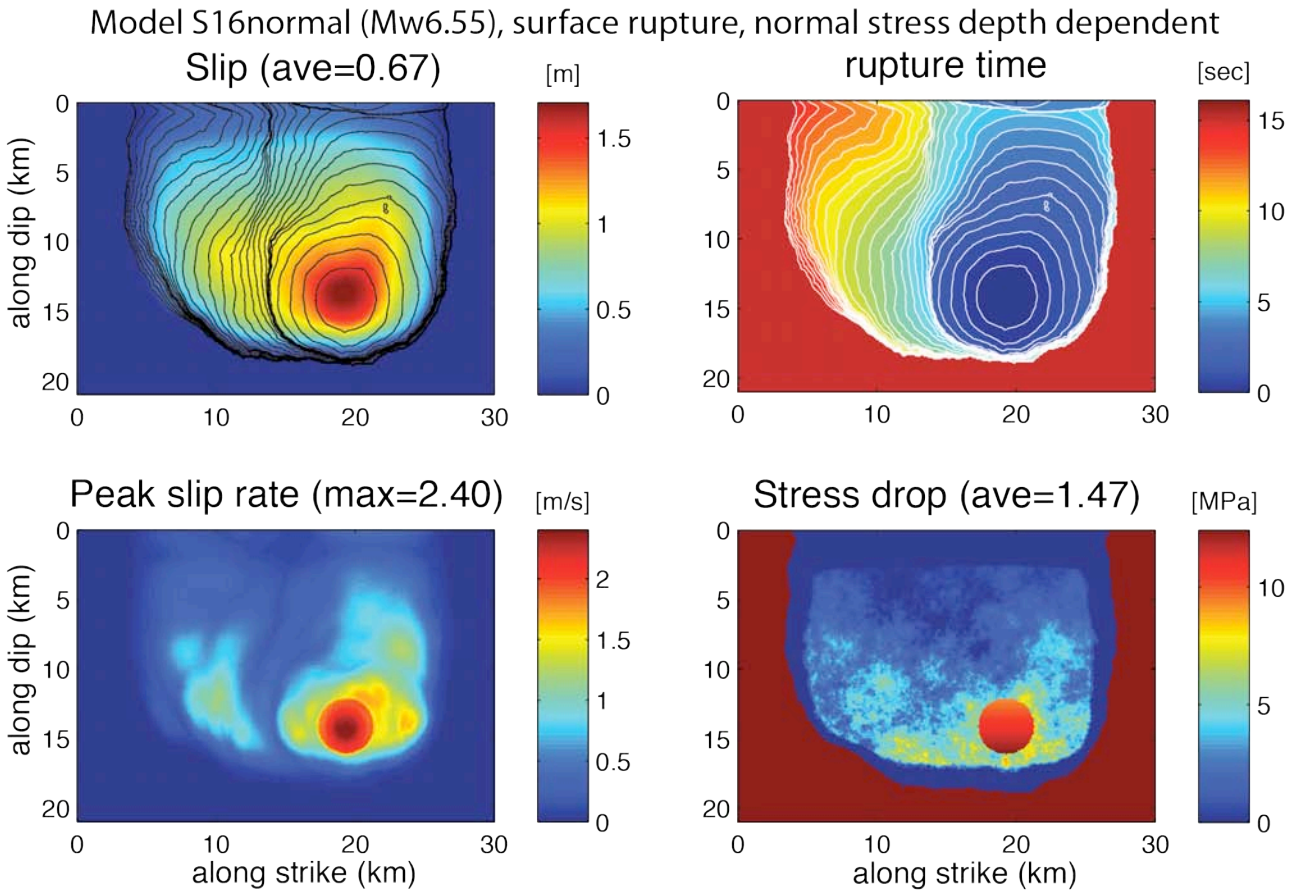

Figure 10. Dynamic rupture solutions for the surface rupturing model "s16normal". Top left shows slip distribution (contour line is the rupture time each 0.5 sec); top right is image map and contour line of rupture time; bottom left is peak slip rate; and bottom right is the stress drop distribution.

Note: In the directory "figures" can be found the original figures from 1 to 6 in format eps, jpg and png.